A STUDY OF SPATIAL VARIABILITY IN SOIL MOISTURE IN A DECIDUOUS FOREST USING ELECTRICAL RESISTIVITY, SOIL TEMPERATURE, AND THROUGHFALL

Ву

Yuteng Ma

A THESIS

Submitted to
Michigan State University
in partial fulfillment of the requirements
for the degree of

Geological Sciences—Master of Science

2014

ABSTRACT

A STUDY OF SPATIAL VARIABILITY IN SOIL MOISTURE IN A DECIDUOUS FOREST **USING**ELECTRICAL RESISTIVITY, SOIL TEMPERATURE, AND THROUGHFALL

By

Yuteng Ma

In deciduous forests, soil moisture is an important driver of energy and carbon cycling, as well as ecosystem dynamics. The amount and distribution of soil moisture also influences soil microbial activity, nutrient fluxes, and groundwater recharge.

Characterizing interactions between vegetation and soil moisture is critical to forecast water resources and ecosystem health in a changing climate. However, these interactions are difficult to measure, both in time and space. Recent studies have shown the ability of electrical resistivity tomography to characterize the spatial and temporal dynamics of soil moisture below a range of different vegetation types. We adopted this method as a main tool to study forest soil moisture. Also, a relatively new and low budget method using *plaster of pairs* was used to capture throughfall.

In this study, an above-ground throughfall measurement is added to the previous below-ground study conducted at the same site years ago to achieve a better understanding of the spatial variability of soil moisture and other environmental variables of a deciduous forest in central Mid-Michigan.

ACKNOWLEDGEMENTS

I would like to express my deepest appreciation and gratitude to all those who gave me the possibility to complete this research. I especially would like to thank my advisor, Remke L. Van Dam, whose knowledge and advice has helped me to achieve my goal. He has spent so much time with me, both in the field and in the lab; without him, none of this would have been possible.

Furthermore, I would also like to acknowledge with much appreciation the crucial role of Michigan State University's Department of Geological Sciences, who gave me permission to use all necessary equipment and material required to complete my research. My committee members, Dr. David W. Hyndman and Dr. Bruno Basso, have generously offered their help at all times. Also, a special thanks goes to my colleagues, Augustin Brena, Alexandria Kuhl, and Ryan Nagelkirk, for their assistance in the field.

Last but not least, I would like to thank my family. My husband, James Loop, has helped me in the field multiple times last summer; but most importantly, his encouragement has sustained me throughout the course of my research. Yingjie Li and Songtao Ma, my parents, have always been very supportive during the process, and I'm so grateful to have had their wisdom and advice.

TABLE OF CONTENTS

LIST OF TABLES	vi
LIST OF FIGURES	vii
Chapter 1 Introduction	1
Objective	4
Chapter 2 Study Site	5
Chapter 3 Methods	10
Vegetation Parameters	10
Vegetation structure	10
Leaf Area Index (LAI)	13
Soil Dynamics	14
Soil temperature	14
Soil moisture from electrical resistivity	15
Setup and data acquisition	15
Data quality	16
Data pre-processing and inversion	17
Temperature correction	19
Water content conversion	20
Climate Variables	21
Air temperature	21
Precipitation and throughfall	22
Precipitation	22
Throughfall	23
Throughfall integrating funnels	24
Chapter 4 Results	27
Soil Dynamics	
Soil temperature analysis	
Temperature corrections of ERI data	
ERI analysis of soil moisture	
Analysis of soil dynamics for short periods	
Tablet period analysis	
Climate variables	
Throughfall from tipping bucket data	
Throughfall from TIFs	

Chapter 5 Discussion and Conclusion	.49
Spatial analysis of vegetation parameters	.49
Vegetation structure and LAI	.50
Spatial and temporal analysis of soil dynamics	.55
Soil moisture and soil moisture changes	
Soil temperature	.57
Geostatistical analysis	
Spatial and temporal analysis of throughfall	
Quantitative Comparisons	.65
Summary	.70
Conclusion	.71
APPENDICES	74
APPENDIX A: Inversion Settings	
APPENDIX B: Tree survey	.77
REFERENCES	78

LIST OF TABLES

Table 2.1: Details on sensor types at the Sandhill site and their typical measurement and download frequencies
Table 4.1: Details of cumulative precipitation during high-precipitation (> 15 mm) weeks (see Figure 4.7a for details)
Table 4.2: Details of cumulative precipitation during low (<5 mm) precipitation weeks (see Figure 4.7b for details)
Table 4.3: Details of cumulative precipitation during tablet periods (see Figure 4.10 for details).
Table 4.4: Coefficients and related data for linear regression models fitted to throughfall and precipitation data
Table B.1: Full detail of the tree vegetation survey at sandhill site75
Table B.2: Summary of vegetation survey in each survey quadrat77

LIST OF FIGURES

Figure 2.1: a) Location of study area in Michigan. b) Aerial view of the Sandhill study site
Figure 2.2: Plot of mean monthly temperature and rainfall for the East Lansing area. A 54-year record (1958 – 2012) of precipitation and temperature were obtained from weatherbase.com
Figure 2.3: Setup of the study site, with locations of resistivity electrodes and the sensors identified in Table 2.1. The central takeout location (between electrodes 42 and 43) is identified with an arrow. The location of one of the three groundwater wells is not shown, as it is a bit further away from the main transect.
Figure 3.1: Layout of eight 9 x 9 m vegetation quadrats at the Sandhill site, showing electrodes 1-50 (black circles) and 17 equally spaced throughfall-integrating funnels (diamonds)1
Figure 3.2: Dimensions measured and estimated for each tree: tree height (TH), crown height (CH), crown base height (CBH), crown diameter (CD) and tree diameter at breast height (DBH).
Figure 3.3: Cross sectional view of one set of apparent resistivity data collected on May 30, 2012
Figure 3.4: Climate variables for the field site, including mean daily air temperature (red line) and daily precipitation during the experiment (blue vertical bars); data were obtained from the MAWN weather station at Hancock Turfgrass Research Center, located 1.5 km from the field site (42.7110, -84.4760). Also shown is the mean daily temperature based on a record from 1980 to 2009 for East Lansing (black line). Green hatched lines indicate dates of table installation and replacement, with gray horizontal lines indicating the total rainfall for each of the tablet periods. The black vertical lines at the top of the graph indicate ERI data collection days
Figure 3.5: a) One of the TIF funnels in the field. b) Tablets before and after use2
Figure 4.1: Vertical temperature profiles in the forest for the days of ERI data collection in a) June, b) July, c) August, d) September, e) October, and f) December
. , , , , , , , , , , , , , , , , , , ,

Figure 4.2: Time series of daily average air temperature from the MAWN weather station for a) June and b) October. The red symbol corresponds to days with apparently anomalous readings in the shallow subsurface (Figure 4.1). Green symbols correspond to other days of ERI data collection
Figure 4.3: Soil temperature profiles for dates surrounding the apparently anomalous temperature reading at 60 cm depth on September 6th
Figure 4.4: Example of temperature curve fitting. a) Second order polynomial function fitted to 4 ibutton readings. b) Linear fit for calculated temperature at 1m depth (based on the polynomial function) and the constant temperature at 10m depth. Note that the horizontal and vertical axes in both graphs are different
Figure 4.5: Temperature profiles for the six dates that coincide with tablet installation and replacement. Temperatures at 5 cm depth (not shown) varied around 20°C for this period while temperature at 1m depth is a lot more similar. The three horizontal dashed lines correspond to the depths (0.25, 0.75, and 1.25 m) of first cells in the resistivity inversion mesh for which temperature correction was applied
Figure 4.6: Distribution of apparent resistivity image points for different a-spacings for the first three vegetation quadrats. The top part of the figure is a plan view showing the vegetation quadrats and electrode locations (black circles); the bottom part of the figure is a side view showing image points below the electrode array
Figure 4.7: a) Weeks with high cumulative precipitation (>15 mm) in between the red lines, which coincide with ERI data collection dates. b) Weeks with low cumulative precipitation (<5 mm) in between the purple lines
Figure 4.8: Percent change in resistivity for time period: May 30 th to June 6 th (top), August 30th to September 6 th (middle) and October 10 th to October 17 th (bottom). The tick marks on the horizontal axis correspond to the boundaries of the 5 vegetation quadrats (Figure 3.1 quadrat 2 to 6)
Figure 4.9: Percent change in resistivity for time period: June 6 th to June 13 th (top) and June 27 th to July 3 rd (bottom)
Figure 4.10: Dates of the tablet experiment (green lines) and daily precipitation throughout the study period.

Figure 4.11: Inverted resistivity of 6 datasets that correlate with tablet swap dates39
Figure 4.12: Water content (cm³/cm³) for the six dates that correlate with the tablet experiment
Figure 4.13: Percent difference in water content for the five tablet periods
Figure 4.14: Rain event characterization based on MAWN hourly precipitation data44
Figure 4.15: Rain intensity (mm/hr) compared with duration (hr)44
Figure 4.16: Relationship between data collected in the forest and grassland45
Figure 4.17: Cross plot of cumulative weight loss versus precipitation for five periods of appoximately four weeks. The lower weight loss fraction in the forest shows the effect of throughfall
Figure 5.1: Tree survey quadrat along with September 26 resistivity profile (Color scale see Figure 4.11)
Figure 5.2: A tree survey shows locations of trees and scaled diameters at breast height. Vegetation quadrat 1 and 7 were not included in the analysis (See Figure 3.1 for sensor locations)
Figure 5.3: Pie chart of the qualitative tree survey
Figure 5.4: Bar graph for each vegetation quadrat with results of the vegetation survey52
Figure 5.5: LAI measurement result and estimated crown area for vegetation quadrats 2 – 652
Figure 5.6: Tree basal area and number of trees in vegetation quadrats 2 – 653
Figure 5.7: a) Six areas of strong negative resistivity changes for the high-precipitation week from October 10 th to 17 th . b) Percent change in soil moisture along the transect for three high-precipitation weeks (Table 4.1). Solid red lines correspond to the areas of high
negative resistivity change area in (a)55

Figure 5.8: Average ERI-derived soil moisture for vegetation survey quadrats 2-6 integrated over a) 0-50 cm, b) 50-100 cm, and c) 100-200 cm depth. Data points are plotted at a horizontal distance representing the middle of each vegetation quadrat; the tick marks represent the edges of the vegetation quadrats.
Figure 5.9: Percent change in soil moisture between table period for vegetation survey quadrats 2-6 (9.75 m to 54.75 m) integrated over a) 0-50 cm, b) 50-100 cm, and c) 100-200 cm depth
Figure 5.10: Average temperature obtained from bi-hourly ibutton temperature readings for the whole study period (red) and five tablet periods
Figure 5.12: Geostatistical analysis on first layer of the resistivity data of six dates that correlate with the tablets replacement dates a) May 30, b) June 27, c) July 25, d) August 30, e) September 26, and f) October 24
Figure 5.13: Temporal evolution of the geostatistical structure of the soil moisture pattern at site, for the datasets previously analyzed. a) mean soil moisture, b) spatial variance, c) range and d) nugget. Red and purple colors are used to highlight high and low precipitation weeks, respectively (see Tables 4.1 and 4.2).
Figure 5.14: Tablet fractional weight loss for each of the TIF locations along the survey transect in the forest. The tick marks represent the edges of the vegetation quadrats64
Figure 5.15: Throughfall depth calculated from tablet weight loss fraction65
Figure 5.16: Comparisons between percent change in soil temperature and soil moisture for dry and wet periods
Figure 5.17: Comparisons between soil temperature and a) crown area, b) LAI and c) basal area.
Figure 5.18: Comparison between soil moisture change and normalized tablet weight loss. Linear regression lines are given for datasets on May-June, June-July and September- October periods

Chapter 1 Introduction

Temperate deciduous forests with four distinct seasons are common in the northern hemisphere (*Hansen et al.*, 2000; *Keddy and Drummond*, 1996; *Wen*, 1999). With the growing population of the world relying on a variety of products and services the forests provide, it becomes critical to properly understand and characterize these systems (*McElrone et al.*, 2013). Previous studies have shown that changes in precipitation, temperature, and other climatic variables, may have important impacts on forest ecosystems, including the type and density of trees (*McKenney-Easterling et al.*, 2000; *Reed and Desanker*, 1992). Furthermore, changes in CO₂ concentration have shown to impact plant water demands and the soil water balance in deciduous forest (*Schafer et al.*, 2002). This makes soil moisture both an indicator and a driver of changes. Thus, understanding near surface soil moisture dynamics is a critical endeavor, especially considering the ongoing and predicted changes in global climate (*Asbjornsen et al.*, 2011; *McKenney-Easterling et al.*, 2000). However, monitoring and quantifying soil water content at relevant spatial scales remain difficult due to the heterogeneities of forest ecosystems.

Soil water content varies temporally as a result of differences in soil water input (precipitation) and output (plant use, evaporation and recharge), driven by seasonal and climatic conditions. Soil water content also changes spatially due to soil texture, vegetation structure, root distribution, and other surface heterogeneities. Over the years, different methods have been proposed to assess the dynamics of these heterogeneous systems, but it remains difficult to integrate measurements of these variables across space and time (*Carlyle-Moses et al.*, 2004).

Interception of precipitation is of critical importance to a forest's soil water balance (Bryant et al., 2005). The loss of precipitation due to canopy interception strongly impacts a forest's hydrological budget (Bryant et al., 2005), as well as influences its nutrient cycles (Michalzik et al., 2001), soil respiration, and gas fluxes (Borken et al., 2006). Interception losses depend on several factors such as canopy storage capacity and the duration and intensity of precipitation events, as well as atmospheric conditions such as wind and relative humidity which influences evaporation rates (e.g. Klaassen, 2001). The relationship between interception (I) and precipitation (P) is usually given as I = P - TF - SF, where TF is throughfall and SF is stemflow (Crockford and Richardson, 2000). Generally, for larger precipitation events, when the canopy storage capacity (CSC) is exceeded, the effect of canopy interception on throughfall becomes insignificant. However, most prior studies of throughfall have shown that it is highly variable in most forests and between forests with different species (Crockford and Richardson, 2000), although some studies have shown distinct patterns, including the effect of canopy interception decreasing with distance from tree stems. In order to get a reasonable estimate of throughfall various methods have been proposed, including randomly spaced rain gauges (Carlyle-Moses et al., 2004) or plastic-sheet rainfall collectors (Crockford and Richardson, 2000).

Soil moisture has traditionally been measured using gravimetric measurements of soil samples. These measurements are generally considered to be accurate, but are time-consuming, invasive, and they offer limited temporal and spatial resolution. Time Domain Reflectometry (TDR) equipment or similar point sensors can also assess soil moisture by obtaining a time series of soil water content and bulk electrical conductivity (*Topp et al.*, 1980), but their invasive nature and limited spatial coverage still makes it not ideal to monitor soil

moisture (*Bréda et al.*, 1995; *Wullschleger et al.*, 1998). These are useful methods to obtain time series of soil water content but have difficulty to obtain data that accurately represent spatial variability. Moreover, these methods are typically sensitive to only a small sampling volume, which makes them prone to errors related to sensor-soil contact.

In recent years, Electrical Resistivity Imaging (ERI) has become a popular method to study spatial and temporal variability in soil properties. It has been used to assess soil moisture (*Jayawickreme*, 2008; *Michot et al.*, 2003; *Zhou et al.*, 2001) soil temperature (*Michot et al.*, 2003; *Pepin et al.*, 1995), soil structure variation as affected by agriculture management (*Basso et al.*, 2012; *Omonode and Vyn*, 2006), and the development of landforms over time (*Van Dam*, 2012). Moreover, ERI was used to study the relationship between vegetation variables and soil moisture (*Garcia-Montiel et al.*, 2008), long-term impacts of land-use conversions on soil-water and groundwater salinity (*Jayawickreme et al.*, 2011), and to monitor water content in weathered bedrock (*Yamakawa et al.*, 2012). However, no study has yet attempted to use ERI in shallow forest soils together with vegetation characteristics and climatic variables to study temporal and spatial variability of soil water.

Objective

The main goal of this research is to improve understanding of relationships in the soilplant-atmosphere continuum in a temperate-climate deciduous forest focusing on
spatiotemporal variability of throughfall and soil water content. In particular, I want to identify
whether the spatial pattern of soil water remains the same during growing season and whether
spatial variability of soil water is correlated to vegetation structure and throughfall. To obtain
insights into these issues, I obtained spatial and temporal estimates of soil moisture using
Electrical Resistivity Imaging in a mature Maple forest in Michigan, USA, for the 2012 growing
season. Vegetation parameters are also measured at the site, including tree density and Leaf
Area Index. Control climate variables were obtained from a nearby weather station while
throughfall was measured at the site.

Chapter 2 Study Site

In this study, I will focus on a single growing season of a maple tree forest in central Lower Michigan (Figure 2.1a). The research took place at the Sandhill area, which is a well-studied research site near East Lansing, Michigan, USA (Figure 2.1b).

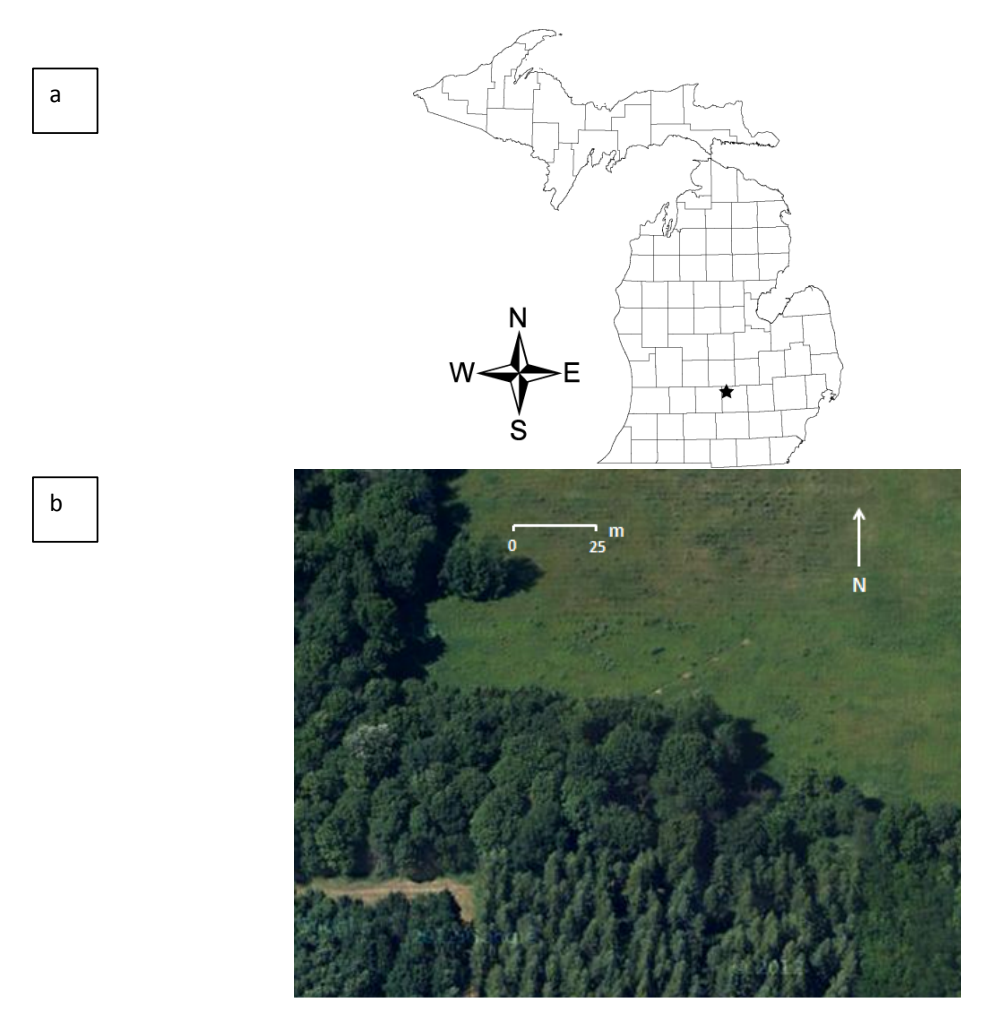


Figure 2.1: a) Location of study area in Michigan. b) Aerial view of the Sandhill study site.

The vegetation at the site consists of a small but mature maple forest (*Acer Saccharum*). The forest has a north-south extent of approximately 50 m and extends from east to west over a distance of at least 200m. Leaf senescence typically starts in October; all leaves will have fallen by Late November, but the exact timing varies from year to year. The forest is bounded to the north by a grassland (Figure 2.1b), which was the subject of previous research by Jayawickreme et al. (2008). The grassland was established in 2004, when a *Honeylocust* (*Gleditsia Triacanthos*) plantation was removed. To the southeast, the study forest is bounded by a pine tree plantation (see Figure 2.1b), while to the southwest, the forest is bounded by a recently cleared forest (still standing in this aerial photograph).

The average precipitation in East Lansing is 760 mm per year (U.S. climate data, 2011). Precipitation occurs throughout the year, with no month with less than 30 mm of precipitation on average. Average precipitation is the largest during the summer months from June through September (Figure 2.2). The July average (maximum) temperature is around 22 (28)°C and the January average (minimum) is around -5 (-10)°C (U.S. climate data, 2011). The difference between mean temperature for the warmest (July) and coldest (January) months is about 26.8 °C (Figure 2.2). On average, there are 174 sunny days per year.

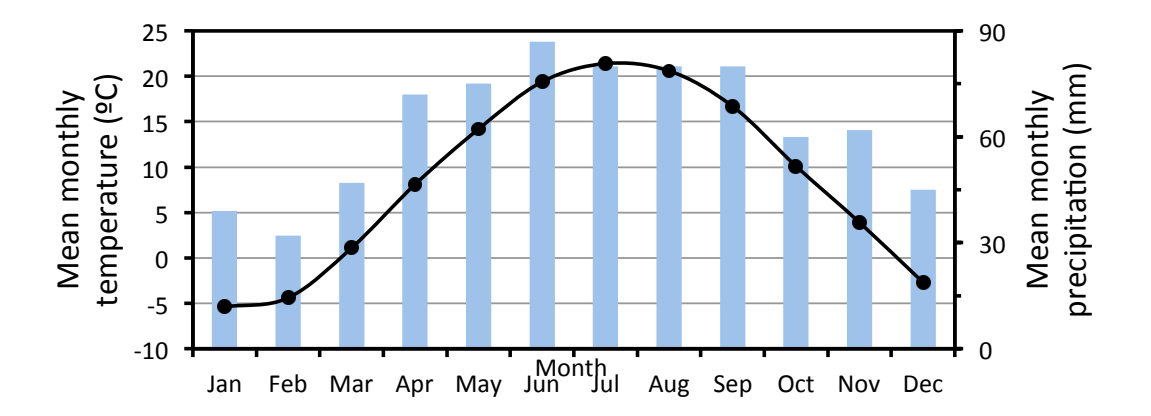


Figure 2.2: Plot of mean monthly temperature and rainfall for the East Lansing area. A 54-year record (1958 – 2012) of precipitation and temperature were obtained from weatherbase.com.

The soils consists of 40-60 cm of clay loam underlain by medium to fine sand, with respective porosities of 0.47 and 0.39 (*Jayawickreme et al.*, 2008). I have assumed that the soil textures and horizons are laterally similar across the studied site. Texture observations from a series of boreholes drilled at the site suggest that this is a reasonable assumption (*Jayawickreme et al.*, 2010). Moreover, in the context of the presented research, which focuses on time-lapse changes, the effect of textural heterogeneity is minimized (more details in the following Chapters).

The Sandhill field site has been used for previous research, which focused on differences in soil moisture dynamics between the forest and grassland vegetation (*Jayawickreme*, 2008). Relatively little attention had been given to the spatial variability within the forest, which is the focus of this thesis. To ensure consistency with the previous work, I use some of the same setup and equipment as had been installed by Jayawickreme (2008). All equipment at the site installed for previous research has had a below-ground focus, with a multi-electrode 2D

resistivity transect, soil moisture point sensors at two depths in the forest and grassland, three shallow groundwater wells, and two vertical temperature arrays with 5 sensors in each (Figure 2.3).

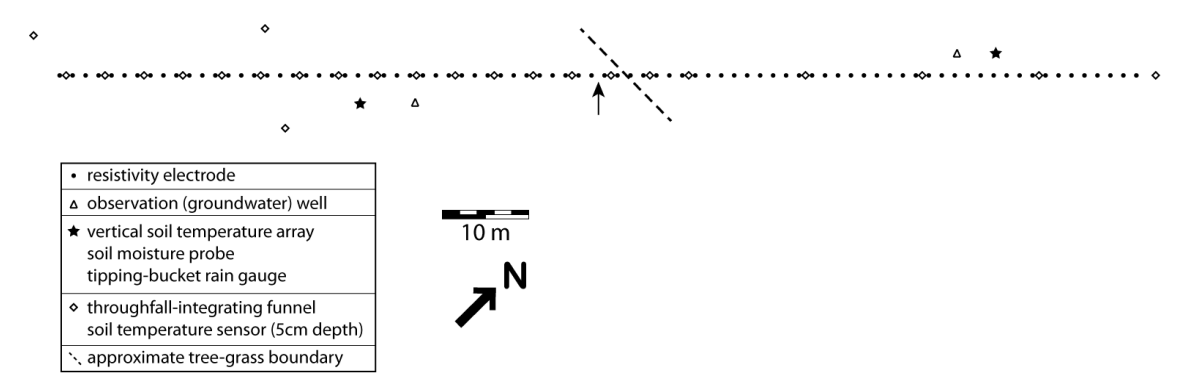


Figure 2.3: Setup of the study site, with locations of resistivity electrodes and the sensors identified in Table 2.1. The central takeout location (between electrodes 42 and 43) is identified with an arrow. The location of one of the three groundwater wells is not shown, as it is a bit further away from the main transect.

For this research, additional data from several above ground sensors was collected, and a few new below ground sensors were installed. The new sensors installed at the site include a tipping bucket rain gauge in the forest and grassland, several so-called 'throughfall integrating funnels', a horizontal array of shallow (5 cm depth) soil temperature sensors, and new vertical soil temperature arrays that replaced the one used by Jayawickreme (2008).

Table 2.1: Details on sensor types at the Sandhill site and their typical measurement and download frequencies.

Measurement	Sensor	Number	Installation date	Collection / download
Electrical resistivity	Electrode AGI	84	October '06	Every Wednesday
Soil moisture	Odyssey	4	Oct '06 & Feb '07	Jan' 13
Temperature (vertical arrays)	iButton	10	Dec '06 & Feb '07	Dec' 12
Temperature (horizontal array)	iButton	24	May & Jun '12	Jan' 13
Water table	Odyssey pressure transducer	3	Sep '07	Jan'13
Rainfall	Throughfall integrating funnel	24	May '12	Every 4 Wednesdays

Table 2.1 (cont'd)

Rainfall	Odyssey tipping	2	Jul' 12	Oct'12
	bucket			
LAI	Decagon LP-80	N/A	N/A	Sep'12

Chapter 3 Methods

Vegetation Parameters

The type and characteristics of forest vegetation has a direct impact on the interception of precipitation, the transpiration of soil water during the growing season, and the blocking of sunlight. Therefore, to understand the potential controls and effects of these variables on throughfall, soil moisture, and soil temperature, a thorough characterization of the vegetation at the site is critical. I conducted a detailed vegetation survey and performed measurements of the Leaf Area Index.

Vegetation structure

A vegetation survey was conducted in June 2013. Eight 9 x 9 m quadrats were set up during the survey, for a total survey area of 648 m^2 . The edges of the survey quadrats coincided with the position of throughfall integrating funnels, which were located in between every third electrode in the forest (Figure 3.1). The position and characteristics of all 42 trees located within this area were measured.

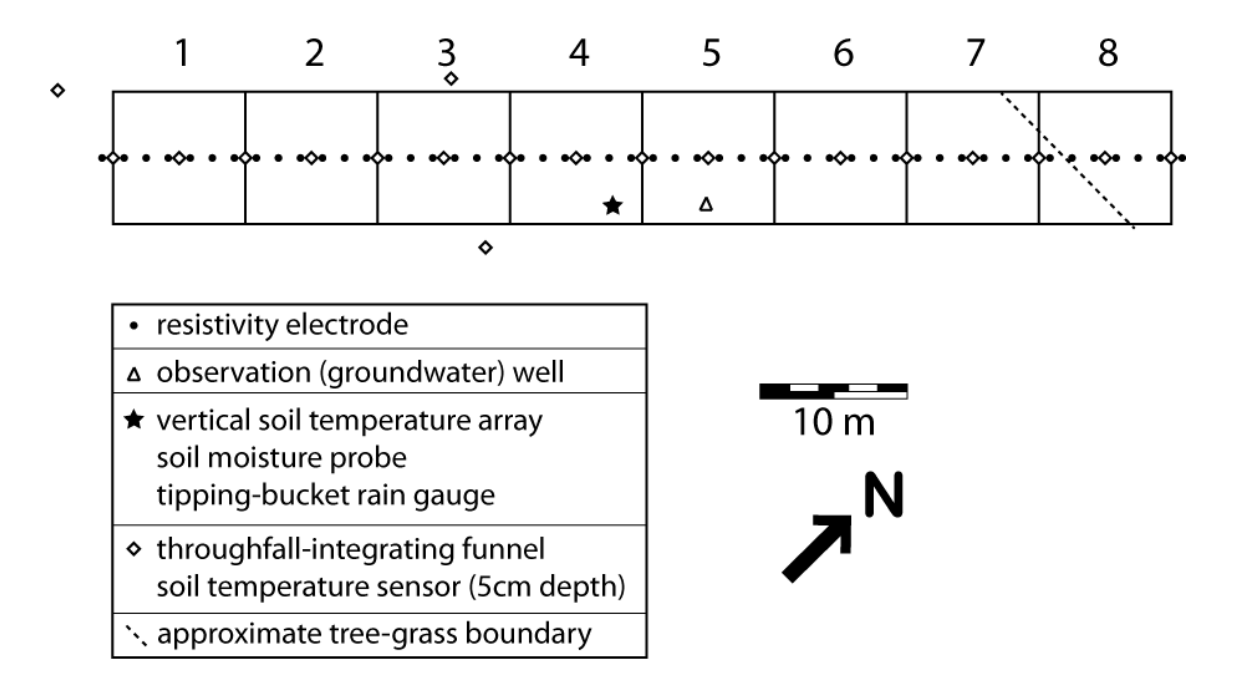


Figure 3.1: Layout of eight 9 x 9 m vegetation quadrats at the Sandhill site, showing electrodes 1-50 (black circles) and 17 equally spaced throughfall-integrating funnels (diamonds).

Following typical vegetation survey procedures (*Montgomery and Chazdon*, 2001) (see Figure 3.2 for terminology) measurements were taken of:

- 1) Number of trees per area. This is typically given in #/100m², so the results for the survey quadrats (81 m²) were corrected to make them easily comparable with literature values. Dead trees (~8% of total) were included in this calculation.
- Diameter at breast height (DBH) for each tree. This value is obtained by measuring the circumference at 1.4 m from the ground. DBH was used to calculate the basal area (BA), which is the total stem area in each survey quadrat. This value is typically given in m²/100m², so the results for the survey quadrats were scaled.

2) Crown diameter (CD) for each tree. The crown of a tree contains the mass of branches growing outward from the tree trunk. The crown diameter is normally obtained as the average of the longest spread and the cross spread oriented at a right angle (90°) from the longest spread. I obtained the CD by measuring the maximum extent of the crown in four radial directions from the trunk; two in opposite directions parallel to the line of electrodes (Figure 3.1) and two in perpendicular directions.

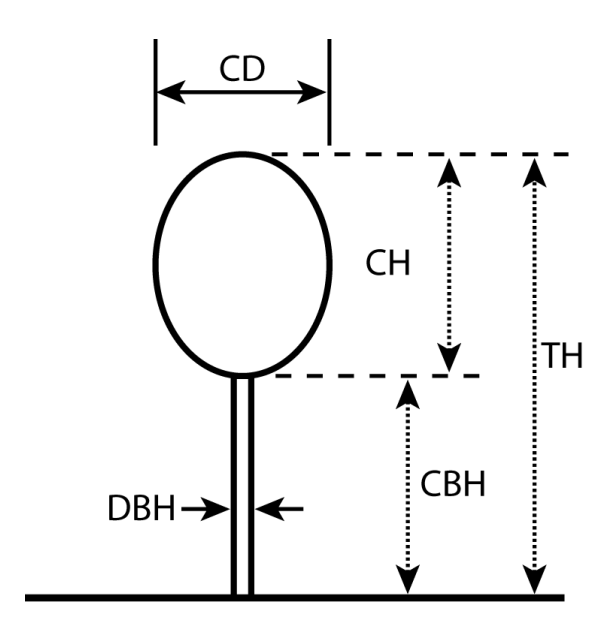


Figure 3.2: Dimensions measured and estimated for each tree: tree height (TH), crown height (CH), crown base height (CBH), crown diameter (CD) and tree diameter at breast height (DBH).

Other typical vegetation measurements, such as tree height (TH), crown depth or height (CH) and crown base height (CBH) were not performed due to the technical difficulty of obtaining reliable results. However, estimates using a laser range finder suggest that most trees were between 25 and 35 m tall. In addition to the above quantitative measurements, several

qualitative observations of each individual tree were taken during the survey. These included tree height (tall or small), living condition (dead or alive), crown size (wide or narrow), and crown depth (deep or shallow; depending on whether the first leafed branch starts lower to or higher from the ground than 50% of tree height, respectively).

Leaf Area Index (LAI)

Watson (1947) first defined Leaf Area Index (LAI) as the one-sided green leaf area per unit ground surface area. It is a dimensionless quantity that characterizes plant canopy. LAI is a key factor for understanding forest ecosystems due to the important role green leaves have in many biological and physical processes (Breda, 2003), including interception, radiation extinction, and water and carbon exchange.

There are two methods to calculate total leaf coverage. The direct measurement method involves collecting leaves below canopy during leaf fall and calculating the leaf coverage for a certain area. This method can be applied to a deciduous forest, but it's destructive, time consuming, and expensive (*Breda*, 2003). The second is the indirect method which uses other variables such as canopy geometry and light interception to calculate LAI (*Blanco and Folegatti*, 2003). I used the indirect method with a Decagon LP-80 in this study. The LP-80 calculates LAI by measuring the light level difference above (or adjacent to) and below the canopy. It takes less time and offers larger spatial coverage. However, in dense canopies LAI values could be underestimated due to the fact that leaves which lie on top of each other will be counted as one leaf according to the theoretical LAI models (*Wilhelm et al.*, 2000).

For a database of measurements (n = 187) for temperate deciduous broadleaf forests from around the world, (*Asner et al.*, 2003) reported LAI values ranging from 1.1 to 8.8, with a mean of 5.1. As part of this research, one LAI survey was conducted at the peak of the growing season. Measurements were conducted at the location of each of the throughfall integrating funnels in the forest (see Figure. 3.1 for locations).

Soil Dynamics

Soil temperature

Soil temperature fluctuates daily and seasonally due to variations in air temperature and solar radiation (*Fayer and Hillel*, 1982), but it is also influenced by soil conditions (texture and moisture content). These fluctuations are important because they impact soil conductivity. As previous research has shown, soil temperature corrections are needed to accurately interpret ERI data in terms of soil moisture content (*Hayley et al.*, 2007; *Jayawickreme et al.*, 2010). Soil temperature also may be a useful indicator of the amount of solar radiation that reaches the soil surface. The input of solar radiation is related to LAI as a lower LAI allows for more sunlight to reach the soil surface. However, due to the varying position of the sun during the day, the area of influence of soil temperature and LAI measurements is different.

Soil temperature was recorded bi-hourly throughout the study period using two different sensor arrays focusing on vertical change and horizontal variability. All temperature arrays used DS1922L ibutton loggers from Maxim Integrated. These loggers have digital thermometers that measure temperature with 0.0625 °C resolution and an accuracy of 0.5°C.

One vertical sensor array was located in the forest, with five sensors at 5, 10, 20, 60, and 100 cm depth (see Figure 3.1 for location). The sensors were placed inside (and made contact

with the side wall of) a PVC pipe that was installed in the ground using a hand auger. The area around the sensors inside the PVC pipe was insulated to prohibit vertical mixing of air. This ensured that the temperature readings were representative of the depth at which the sensors were installed. Data were accessed for download without removing the PVC tubes from the ground and the ibutton loggers from their position in the tube. Data from these sensors were used to construct vertical temperature profiles at the time of resistivity data collection.

The spatial distribution of soil temperature was measured using identical ibutton thermometer loggers located 5 cm below the surface, directly adjacent to (on the south side of) each throughfall integrating funnel (see Figure 3.1 for locations).

Soil moisture from electrical resistivity

Setup and data acquisition

A 124.5 m long electrode array centered on the forest-grassland boundary was first installed in 2006 to monitor vegetation and climate impact on soil moisture. 84 permanent graphite electrodes (Φ 1.2 cm x 30 cm) were placed at 1.5 m spacing and with underground wiring to a central takeout point (see Figure 2.3). An AGI SuperSting R8 IP eight-channel earth resistivity meter and a switch box for 84 passive electrodes were brought to the field for data collection. 24 individual electrical resistivity datasets were collected during the study period from May to December 2012. Each dataset took approximately 150 minutes to collect, resulting in 1134 subsurface apparent resistivity measurements with Wenner configuration and 1234 measurements with dipole-dipole configuration. For this study, only the Wenner configuration data from the forest portion of the transect was analyzed. (2008). In the middle of the study

period, the underground wire to electrodes 79 - 84 was broken for a short period of time. This yielded fewer data points in three datasets, but because these electrodes were located in the grassland section of the transect, this had no effect on the interpretation of resistivity variation in the forest. Figure 3.3 is a cross sectional view of the resistivity distribution of the study site early in the study period illustrating subsurface apparent resistivity differences below the two land covers. For this thesis, data analysis was based on only the 44 electrodes located below the forest canopy. This resulted in a total of 301 apparent resistivity readings with Wenner array for each time period.

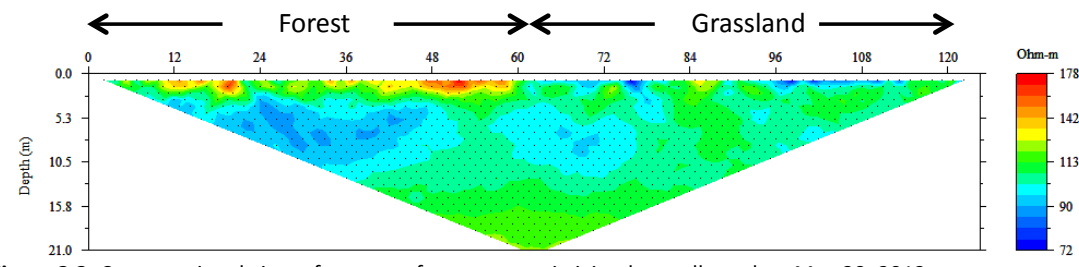


Figure 3.3: Cross sectional view of one set of apparent resistivity data collected on May 30, 2012.

Data quality

Previous work at this site has shown that data quality is very high with less than 0.2% of data failing a tight repeat error criterion of 1% (*Jayawickreme et al.*, 2010). These repeat errors did not correlate significantly with environmental variables (e.g., precipitation events, air temperature). In this study, no repeat measurements were collected to limit the overall survey time. Also no reciprocal data were collected, but data from a nearby site with similar soil type, comparable setup and data collection procedures had an average reciprocal error of 0.33% (n = 289 with a-spacings of 0.75 to 13.5 m). The contact resistance is an additional indicator of data quality and these data were collected during each field survey. An analysis of contact resistance

data from six datasets throughout the growing season (n = 1806) shows that there is no systematic correlation with electrode location or a-spacing, indicating consistent data quality. The average contact resistance did increase during the growing season, as would be expected as the soil dried out.

Data pre-processing and inversion

Resistivity data were analyzed using AGI 2D Earth Imager software. The first step of the data analysis procedure is to eliminate bad data, which may come from broken electrodes or other possible influences along the study line.

Inversion settings are given in Appendix A. Some important settings include the number of mesh divisions, starting model, and error reduction. In this case, a constant 50 x 50 cm mesh was used. To account for edge effects, so-called "padding cells" of increasing size with distance from the model domain were used along the left, right, and bottom boundaries of the inversion quadrat. The pseudosection was used as the starting (reference) model. As shown by (*Eustice*, 2008), a peudosection starting model results in a better characterization of sharp electrical transitions, such as the water table, compared to a start with a homogeneous starting model such as the average resistivity.

One of the main reasons to install the electrode array permanently is to take advantage of its improved repeatability of measurements, which improves the signal-to-noise ratio for time-lapse resistivity surveys. To obtain insight in the temporal dynamics at the site, I analyzed the difference between individual datasets. Different procedures for inverting time-lapse geophysical data have been proposed (*Hayley et al.*, 2009; *LaBrecque and Yang*, 2001; Miller et al., 2008) including: (a) using one inverted model from a base data set as a reference model for

following time periods, (b) inverting the difference between two apparent resistivity datasets, and (c) subtracting resistivity models (inversion results) after inverting two datasets separately.

Jayawickreme et al. (2008) used the first approach with a base model as the reference model to invert monitoring datasets and to obtain estimates of the differences between two data sets. A potential disadvantage of this method is the large impact of the choice of base dataset on the resulting differences (*Jayawickreme et al.*, 2010, Figure 4). Another potential disadvantage is the possibility of error propagation in datasets with non-systematic data errors (*Jayawickreme et al.*, 2010; *Miller et al.*, 2008) also pointed out some potential issues with the second approach.

In this study, I used the third inversion approach by inverting the data sets independently and subtracting the resulting models to obtain the difference. Potential drawbacks of this approach include the non-uniqueness of individual inversions and the possibility that small errors in the data produce incorrect resistivity changes or mask actual resistivity changes (*Daily and Ramirez.*, 2005; *Jayawickreme et al.*, 2010). However, it has also been suggested that this approach is in fact preferred over the difference inversion approach used by Jayawickreme et al. (2008) because it's not as sensitive as difference approach, which requires well understood and quantified data noise (*Miller et al.*, 2008). All inversions were halted at the same iteration step. This procedure provides a comparable heterogeneity in each resistivity model and improves the ability to compare the spatial distribution of resistivity and water content over time.

The study site has a slight increase in elevation along the transect from forest to grassland. The maximum topographic change between individual electrodes is less than 10 cm.

Hennig et al. (2005) found out that under certain circumstances, for example using half-Wenner configuration with a flank angle less than 25°, topographic correction can be neglected. The elevation difference along the line compared with the 124.5 m horizontal line and 0.1 m maximum elevation between electrodes makes the topographic effect trivial. Since trial inversions with and without topographic correction produced no significantly different results, no topographic correction was applied for the data in this thesis.

Temperature correction

The influence of temperature on measured apparent resistivity can be removed using empirical models. A linear model was used in this study to correct for the temperature effect, similar as in Jayawickreme et al. (2010). According to Sen and Goode (1992), the resistivity at a base (reference) temperature can be calculated using:

$$\frac{\rho_{ref}}{\rho_t} = c(t - t_{ref}) + 1, \tag{3-1}$$

where ρ_{ref} is the resistivity at a reference temperature (usually at 25°C) and ρ_t is the measured resistivity at temperature T. c is the fractional change in resistivity per unit change in temperature. This value is a constant over the temperature range of interest, but appears to be nonlinear at larger temperature ranges. I used a value of 0.018, similar as in Jayawickreme (2008), based on observations from 2°C to 20°C for glacial till materials (*Hayley et al.*, 2007).

Temperature corrections were performed after inverting the measured apparent resistivities using temperature data obtained directly from the temperature ibutton loggers. A different approach for temperature corrections was proposed by Hayley et al. (2010), who

argued that correction after inversion might lead to an underprediction of EC changes (and thus soil moisture), due to the use of smoothness constraints, especially when using a homogeneous starting (reference) model. In this study, which used the pseudosection starting model the correction-after-inversion approach was used. This ensured consistency with previous work at this site (*Jayawickreme*, 2008; *Jayawickreme et al.*, 2008; *Jayawickreme et al.*, 2010). For the conversion, I used the ibutton sensors at 20, 40, 60, and 100 cm depth, with the temperature reading closest in time to ERI data collection. Temperature was assumed to be constant at 10.25°C at 10 m depth after Jayawickreme et al. (2010). No spatial variability in soil temperature was incorporated in this correction. To get a better understanding of the validity of this assumption, the 5-cm depth temperature probes along the transect were analyzed (results shown in Chapter 5).

Water content conversion

In order to understand soil moisture distribution in space and its dynamics in time, the resistivity models obtained through inversion and after correction for the temperature effect need to be converted to water content. Previous work has shown an excellent correlation at the site between ERI-derived moisture values with independently obtained volumetric water content readings, although this work also showed that the ERI slightly under-estimates soil moisture (See Figure 8, Jayawickreme et al. 2010). The relationship between electrical resistivity and water content is well known to be soil-specific (*Gupta and Hanks*, 1972). However, there have been a few efforts in recent years to establish generally accepted pedotransfer functions (*Hadzick et al.*, 2011) as they commonly exist to estimate soil moisture from ground-penetrating radar data (*Steelman and Endres*, 2011; *Van Dam*, 2013). To estimate

soil water content from resistivity in this study, I use site and material specific relationships between resistivity (ρ) and water content (Θ) that were developed following ASTM standard G57-95, which is based on the Archie equation (*Archie*, 1942):

$$S = \left(\frac{\rho_S}{\rho}\right)^{\frac{1}{m}},$$
 3-2

where S is the saturation (water content/porosity) and ρ_s is the bulk resistivity of soil at 100% saturation. Based on the lab results, most of the soil materials tested fit the ρ - Θ Archie function. The m value was estimated as 1.16 for sand and 0.67 for clay, and ρ_s is 71.53 Ω m and 68.15 Ω m, respectively (Jayawickreme et al., 2008). After the resistivity data were inverted and corrected for the temperature effect the soil water content was calculated.

In dry unsaturated areas, the fluid conductivity has a smaller effect on bulk resistivity than water saturation. Based on the fact that the annual precipitation in Michigan exceeds evapotranspiration, Jayawickreme et al. (2010) argued that fluid conductivity from the water table has minimal impact on the water content estimations.

Climate Variables

Air temperature

Hourly air temperature and precipitation data were obtained from a weather station of the Michigan Automated Weather Network (MAWN), located 1.5 km away, at the Hancock Turfgrass Research Center at MSU, East Lansing. Mean daily air temperature increased from

the start of the study period to a peak in July; it then gradually decreased throughout the rest of the study period (Figure 3.4).

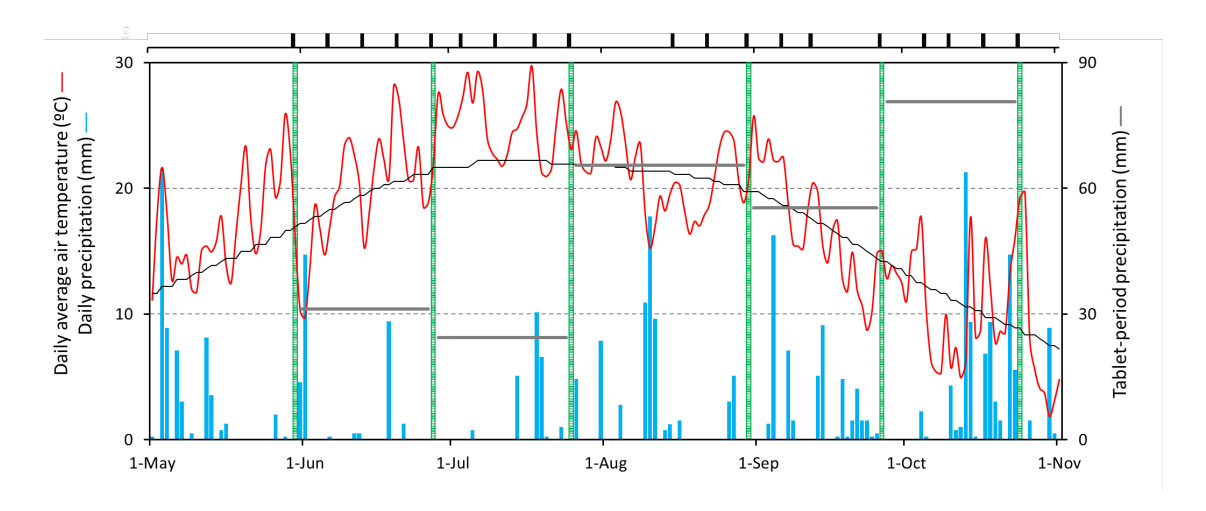


Figure 3.4: Climate variables for the field site, including mean daily air temperature (red line) and daily precipitation during the experiment (blue vertical bars); data were obtained from the MAWN weather station at Hancock Turfgrass Research Center, located 1.5 km from the field site (42.7110, -84.4760). Also shown is the mean daily temperature based on a record from 1980 to 2009 for East Lansing (black line). Green hatched lines indicate dates of tablet installation and replacement, with gray horizontal lines indicating the total rainfall for each of the tablet periods. The black vertical lines at the top of the graph indicate ERI data collection days.

Precipitation and throughfall

Precipitation

Hourly precipitation data from the MAWN station was analyzed to characterize the rainfall intensity for individual events, and as daily totals, to compare with the tipping bucket rain gauge data and with the TIF results. The daily precipitation shows a predominantly dry period at the beginning of the study period, from the middle of May through July. From late July to November various more significant precipitation events were observed (Figure 3.4).

In addition to the MAWN station, precipitation information was obtained from a tipping bucket rain gauge in the grassland (see Figure 2.3 for location). The tipping bucket rain gauge measured every 0.2 mm rainfall at the exact time of the bucket drop. Data from this tipping bucket gauge does not cover the entire data period as it suffered from a few outages. It therefore cannot be used to analyze the entire period. However, it can still be effectively used to evaluate differences between precipitation measured at the site and the MAWN data. To this end, I compared the results from the gauge in the grassland (no interception) with the rainfall data from the MAWN weather station.

Throughfall

The interception characteristics of a forest can be hard to identify and quantify (*Crockford and Richardson*, 2000). The factors that affect interception include: (a) forest type and location, including canopy storage capacity, leaf area index, storage capacity of shrub and litter layers, hydrophobicity of leaf and wood, and projection of tree crowns, and (b) climatic factors, including the amount, intensity, duration, and angle of rainfall, wind speed and directions, and air temperature and humidity. There are so many variables that make it extremely challenging to accurately measure interception. In this study, I measured throughfall as an indicator of interception while stemflow was neglected. This is similar to work by (*Liu*, 1997), where stemflow wasn't considered. Also, Dolman (1987) found stemflow can be neglible during foliate periods in a study of an oak forest. Given the annual precipitation (760 mm) and maple being the dominate tree species, I decided to adopt this simplified method that doesn't measure stemflow and relies on accurate precipitation and throughfall measurements.

To study the general effects of the forest canopy on rainfall interception and throughfall I used a second tipping-bucket rain gauge that was installed in the forest along the electrode line (see Figures 2.3 and 3.1 for location; Table 2.1 has details). This tipping-bucket collected data in identical fashion to the one in the grassland; it also suffered from a few outages.

The difference in input recorded between the rain gauges in the forest and the grassland is due to interception losses. I analyzed the effect of precipitation intensity and duration on this relationship, which is expected to be influenced by the canopy storage capacity (CSC). For significant rainfall events where CSC is exceeded, the throughfall fraction is expected to be larger than for small events (Crockford and Richardson, 2000).

Throughfall integrating funnels

To study the effects of forest interception on the spatial variability in throughfall, I used a novel and low-budget method, called Throughfall Integrating Funnels (TIF). This method was used to quantify the cumulative throughfall in approximately 4-week intervals. In this method, which was proposed by *Dunkerley*, (2010) and used in different studies *Ma et al.*, 2014), precipitation (or throughfall) is collected in a funnel and guided over a calcium sulphate hemihydrate tablet ("plaster of paris") (Figure 3.5). As water flows over the tablet, some calcium sulphate dissolves. The weight loss is expected to correlate with the quantity of water that flowed over the tablet.





Figure 3.5: a) One of the TIF funnels in the field. b) Tablets before and after use.

Because the weight loss associated with a single precipitation event is small, Dunkerley (2010) suggested using this approach to measure longer-term effects. Thus, the weight loss measured over a period of a few weeks can represent the amount of water guided over the tablet in that period. Therefore, this method cannot be used to assess the effect of individual events (including intensity and duration). However, it may be an effective method to quantify long-term moisture inputs to the forest floor.

In May 2012, a set of 24 TIFs was installed (see Figure 2.3 for location). TIFs #1 through #15 were 4.5 m apart under the canopy in the maple forest. Funnel #16 is centered on the border between the forest and the grassland, under the drip-line. Funnels #17 through #21 were placed 12 m apart from each other above the grassland. Funnels #22 through #24 were placed at specific locations in the forest, either close to certain trees or in relatively open space. All TIFs were installed with the funnel opening at approximately 65 cm above the ground except for #10, which has a height of ~100 cm above the soil surface. The TIFs in the grassland are above the canopy and should therefore measure cumulative precipitation, whereas the TIFs in the forest are expected to produce lower weight loss due to precipitation interception.

Tablets were made in the lab with a small Teflon baking tray in batches of 24. Two parts of Plaster of Paris and one part of water were used as suggested. The mixture was thoroughly stirred using a spatula attached to a power drill until no clumps were noticeable. The mixture was then was poured into the baking tray. Initial hardening of the tables normally took 2 hours. Before field installation, the tablets were oven-dried at 120 °C for 24 hours, weighed on a standard lab scale with high precision (weight in grams with three significant digits), and then immediately installed in the field to avoid moisture contamination during the process. After the measurement interval, each tablet was removed from the field and replaced with a new one. The removed tablets were dried in the same oven at the same temperature setting, and then weighed again. The weight loss recorded during each study period is expected to be proportional to the volume of water that has passed over the tablet during that time period. This relationship may be affected by rainfall intensity (changing the amount of tablet each drop would come in contact with the tablet) and duration (possibly saturating the tablet, and thus changing conditions for long duration events). It is, however, very difficult to test for this effect as the tablets were left in the field for 4-week periods and were thus exposed to different types of precipitation events. The throughfall fraction TF_f was obtained by comparing the weight loss under the forest canopy to the weight loss of the grassland tablets.

Chapter 4 Results

In this chapter, I will analyze soil moisture data as well as climate variables. Temperature analysis is critical for obtaining accurate resistivity results. To begin this chapter, I will present how I derived temperature correction functions and how I used them in correcting resistivity data. After that, I will describe resistivity and soil moisture changes for several short (~ 1 week) periods (both dry and wet) as well as the results of resistivity mapping that covers several longer periods (coinciding with tablet datasets of throughfall). In addition to presenting the results, data quality will also be addressed at each subsection.

Soil Dynamics

Soil temperature analysis

Throughout the study period, two temperature arrays in the forest and the grassland, with sensors at 5, 20, 40, 60 and 100 cm depth, were used to capture subsurface temperature changes. These measurements are used to perform temperature corrections of the individual resistivity data. Figure 4.1 shows temperature profiles in the forest for the days when ERI data was collected. In July, August and November (Figure 1b, 1c, and 1f) the temperature curves for all the datasets collected within that month are very consistent. Only a few temperature data appear anomalous, including those on June 13th (low temperatures at 5 and 20 cm depth; Figure 1a), September 6th (high temperature at 60 cm depth; Figure 1d) and October 10th (high temperatures at 5 and 20 cm depth; Figure 1e).

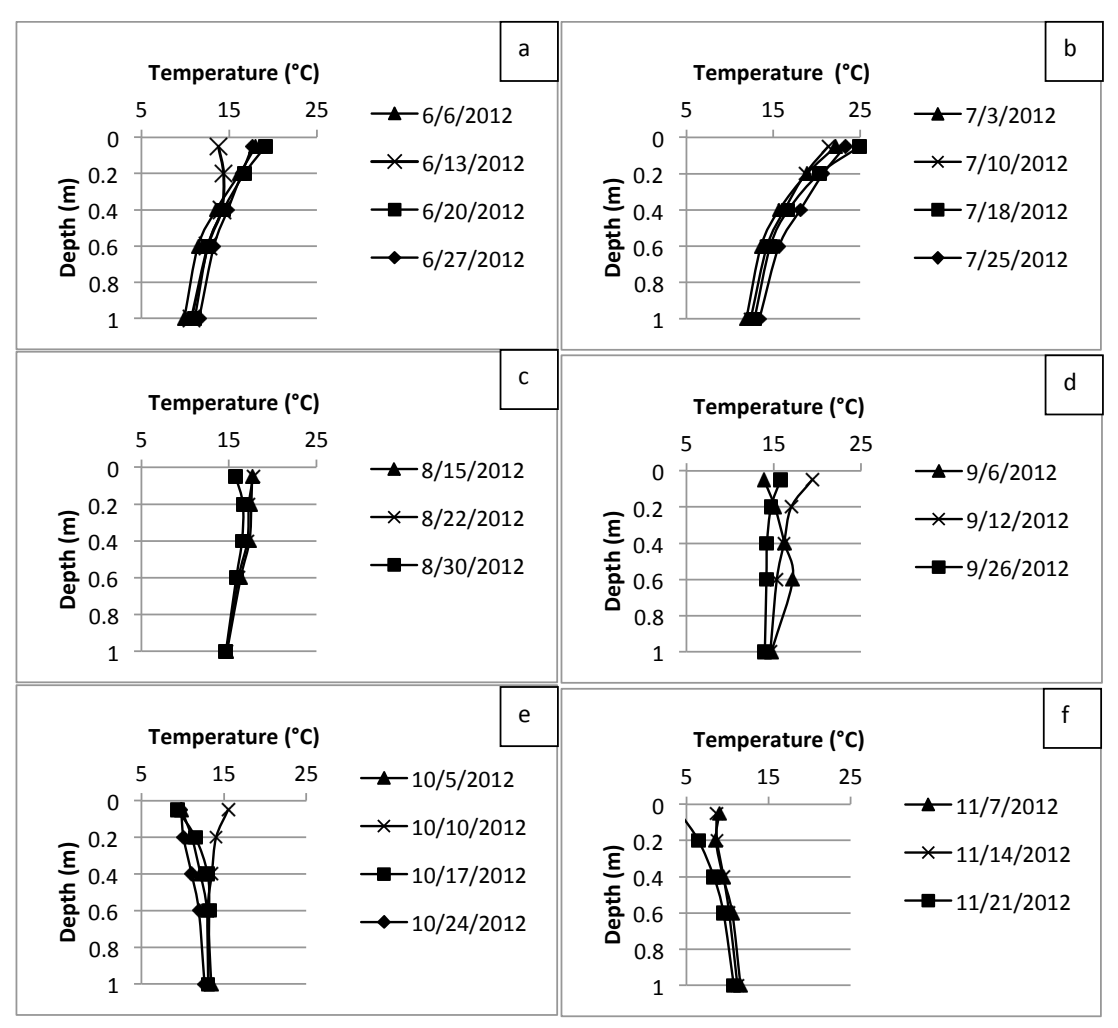


Figure 4.1: Vertical temperature profiles in the forest for the days of ERI data collection in a) June, b) July, c) August, d) September, e) October, and f) December.

To check the accuracy of the apparently "anomalous" readings, they were compared with daily average air temperatures and soil temperature data for preceding and following days. The June 13th data collection date is preceded by several relatively cold days (Figure 4.2a), explaining the low temperature measured in the 5- and 20 cm loggers on that day (Figure 4.1a). In contrast, the data from October 10th was preceded by several days with anomalously high air temperatures (Figure 4.2b) indicating that the measured data (Figure 4.1e) are accurate. To

validate the apparently anomalous reading on September 6th (Figure 4.1d), I plotted 7 days of soil temperature data from September 3rd to 9th (Figure 4.3). Despite the near surface variations, all the datasets show that at 0.6 m depth the temperature is around 16°C. These three graphs proved none of them were anomalies and validate the use of temperature collected by the arrays for correction purpose.

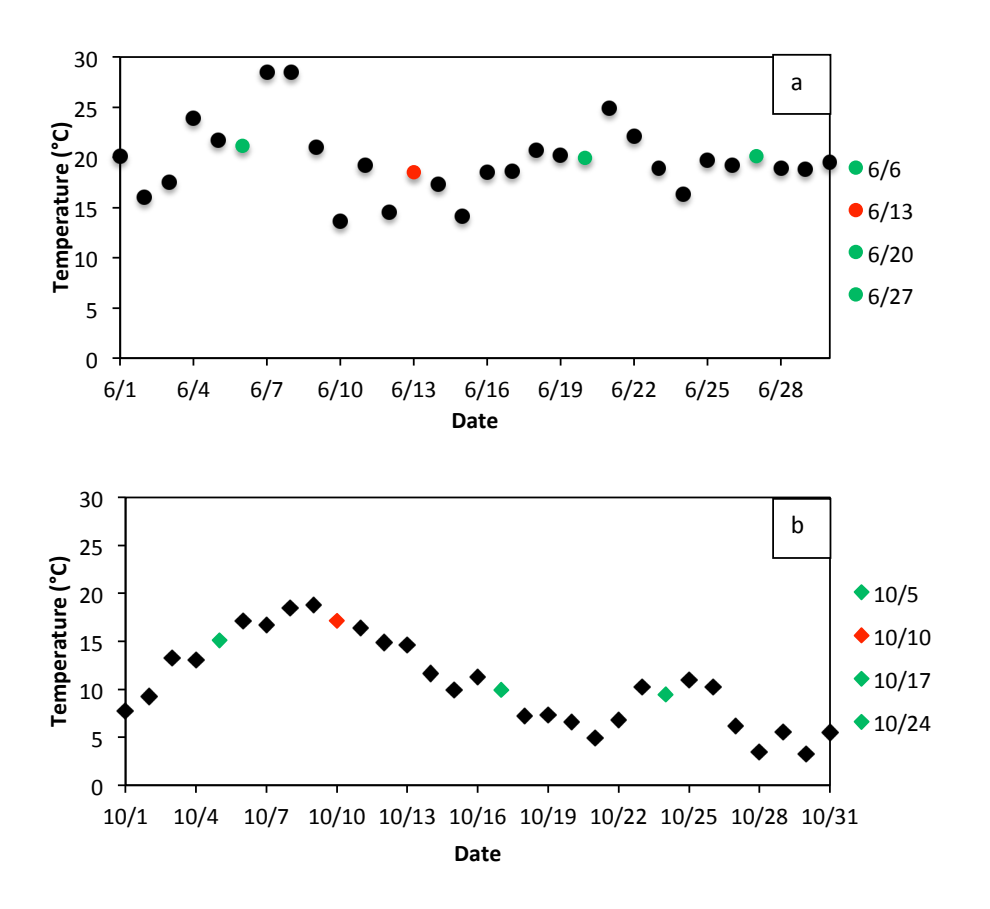


Figure 4.2: Time series of daily average air temperature from the MAWN weather station for a) June and b) October. The red symbol corresponds to days with apparently anomalous readings in the shallow subsurface (Figure 4.1). Green symbols correspond to other days of ERI data collection.

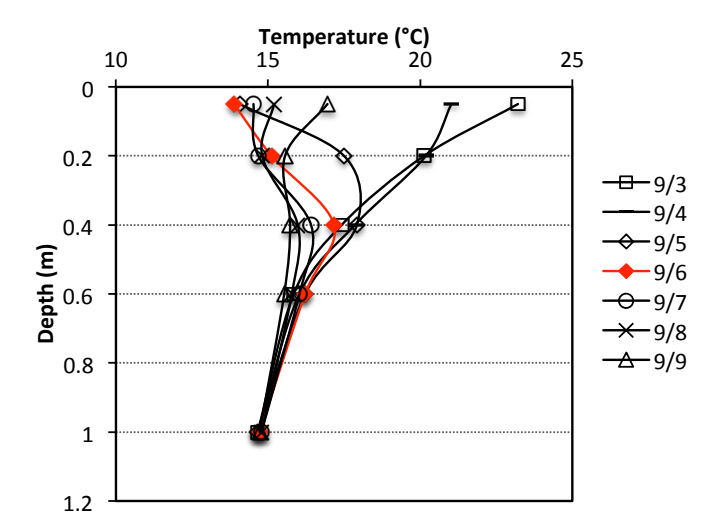


Figure 4.3: Soil temperature profiles for dates surrounding the apparently anomalous temperature reading at 60 cm depth on September 6th.

Temperature corrections of ERI data

According to (*Hayley et al.*, 2007), soluble materials and spatial variations in chemistry may have less of an impact on soil electrical conductivity (reciprocal of electrical resistivity) than temperature variations in the near surface area. (*Rein et al.*, 2004) have pointed out that even daytime temperature variations can have large impacts on soil electrical resistivity. Electrical conductivity is usually expressed at a reference temperature of 25°C. Among all the different types of models that describe the relationship between temperature and soil electrical conductivity, Hayley et al. (2007)'s model is chosen to be used in this research:

$$\sigma_{std=(\frac{m(T_{std}-25)+1}{m(T_i-25)+1})\sigma_i}$$

Where, T_{std} is a reference temperature, σ_{std} is conductivity at the reference temperature, T_i and σ_i are the measured temperatures and electrical conductivity values, respectively, and m is a material dependent temperature coefficient.

Jayawickreme et al., (2010) concluded that at this study site, the effect of temperature is larger in lower resistivity ranges near soil water saturation. They estimated that a 12°C temperature change could lead up to 20% difference in calculated soil moisture. During the study period in 2012, temperature differences of this magnitude were observed at shallow depths, with the highest readings generally in July (Fig. 4.1b) and the lowest in November (Fig. 4.1f)

To correct resistivity inversion results at depths without ibuttons, I fitted curves to the measured temperature array data. Data at 5 cm was ignored to minimize the impact of short-term fluctuations near the soil surface. My temperature correction consists two parts: a second-order polynomial function above 1 m depth based on ibutton readings and a linear function from 1 m depth up to a constant temperature of 10.25°C at 10 m (as in Jayawickreme et al., 2010). The calculated temperature at 1m (using the polynomial function) was used as input for the linear function. This avoids an unnecessary temperature jump at 1m when using the measured temperature instead. Figure 4.4 is an example of obtaining temperature correction functions using a dataset collected on June 26th. Figure 4.5 has the temperature correction profiles for six of the resistivity data collection dates that coincide with the tablet installation and replacement days (see Fig. 3.4).

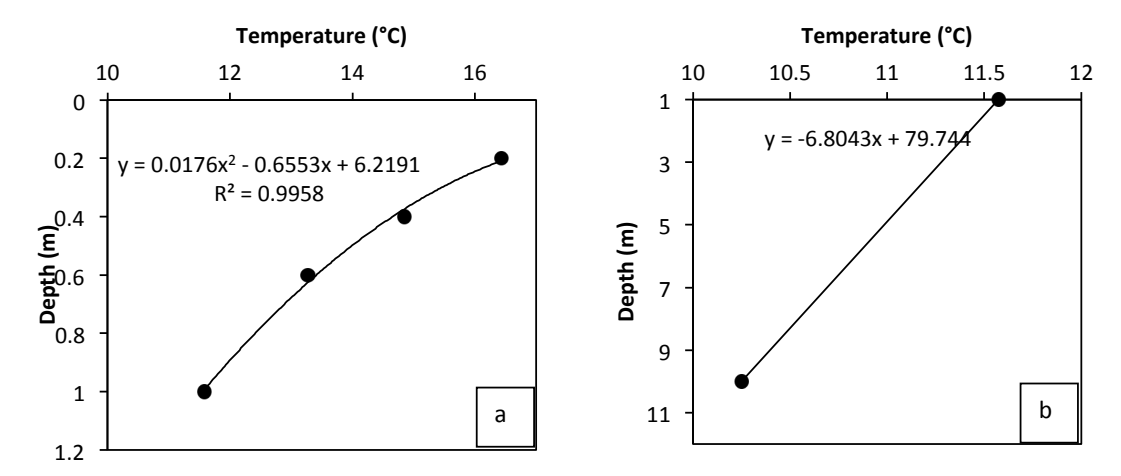


Figure 4.4: Example of temperature curve fitting. a) Second order polynomial function fitted to 4 ibutton readings. b) Linear fit for calculated temperature at 1m depth (based on the polynomial function) and the constant temperature at 10m depth. Note that the horizontal and vertical axes in both graphs are different.

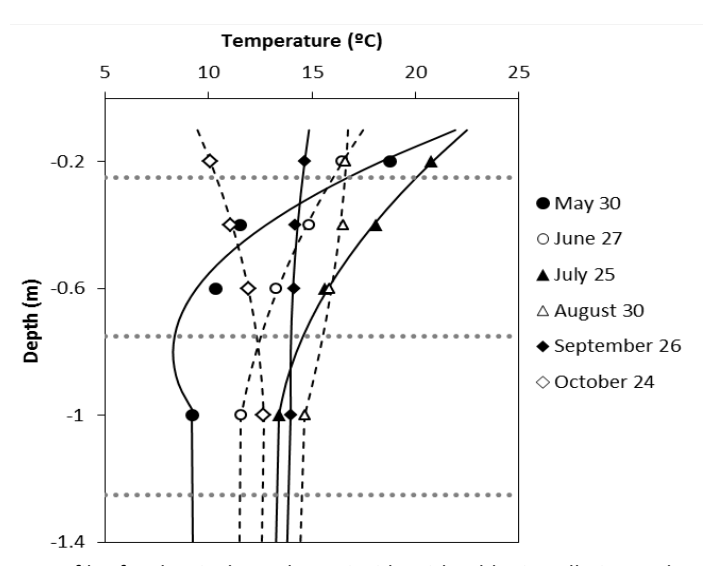


Figure 4.5: Temperature profiles for the six dates that coincide with tablet installation and replacement. Temperatures at 5 cm depth (not shown) varied around 20°C for this period while temperature at 1m depth is a lot more similar. The three horizontal dashed lines correspond to the depths (0.25, 0.75, and 1.25 m) of first cells in the resistivity inversion mesh for which temperature correction was applied.

ERI analysis of soil moisture

The study period of 2012 is a relatively dry growing season. Soil moisture deficit was observed in the most of the datasets, this has happened for other years at this site (Jayawickreme, 2008; Jayawickreme et al., 2010). Several major rain events occurred later in the growing season, which helped to recover the deficit.

All the results figures will focus on the vegetation survey quadrats 2 to 6 (for the quadrat layout see Figure 2.3 and Figure 3.1). Vegetation quadrat 1 was eliminated from the analysis because although it has electrodes throughout the whole quadrat (Figure 4.6; top), it is only partially covered by resistivity image points (Figure 4.6; bottom). Thus, the analysis of soil moisture both spatially and temporally would not be accurate for this quadrat. All the soil moisture analysis will therefore start at 9.75 m and end at 54.75 m and only covers vegetation quadrat 2 to 6. The depth range will be 5 m for the plots of resistivity inversion; the difference analysis will only contain the first 2 m of depth to better focus on the depth range in the subsurface where most changes occur.

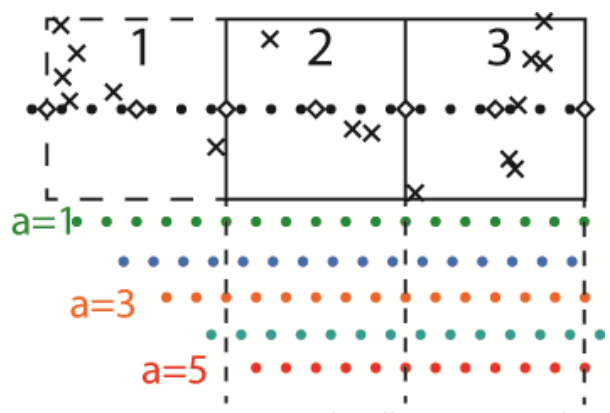


Figure 4.6: Distribution of apparent resistivity image points for different a-spacings for the first three vegetation quadrats. The top part of the figure is a plan view showing the vegetation quadrats and electrode locations (black circles); the bottom part of the figure is a side view showing image points below the electrode array.

Analysis of soil dynamics for short periods

During the study period approximately weekly ERI datasets were collected, with a few missing data collection periods. Based on the data collection dates, I categorized weeks with high (>15 mm) and low (<5 mm) cumulative precipitation (Tables 4.1 and 4.2). All precipitation data for this analysis was obtained from the MAWN weather station. The cumulative precipitation for the tablet periods (Table 4.3) was calculated in similar fashion. Figure 4.7 shows the rain events during the study period. Data collection dates at the start of wet and dry weeks have been indicated with vertical lines

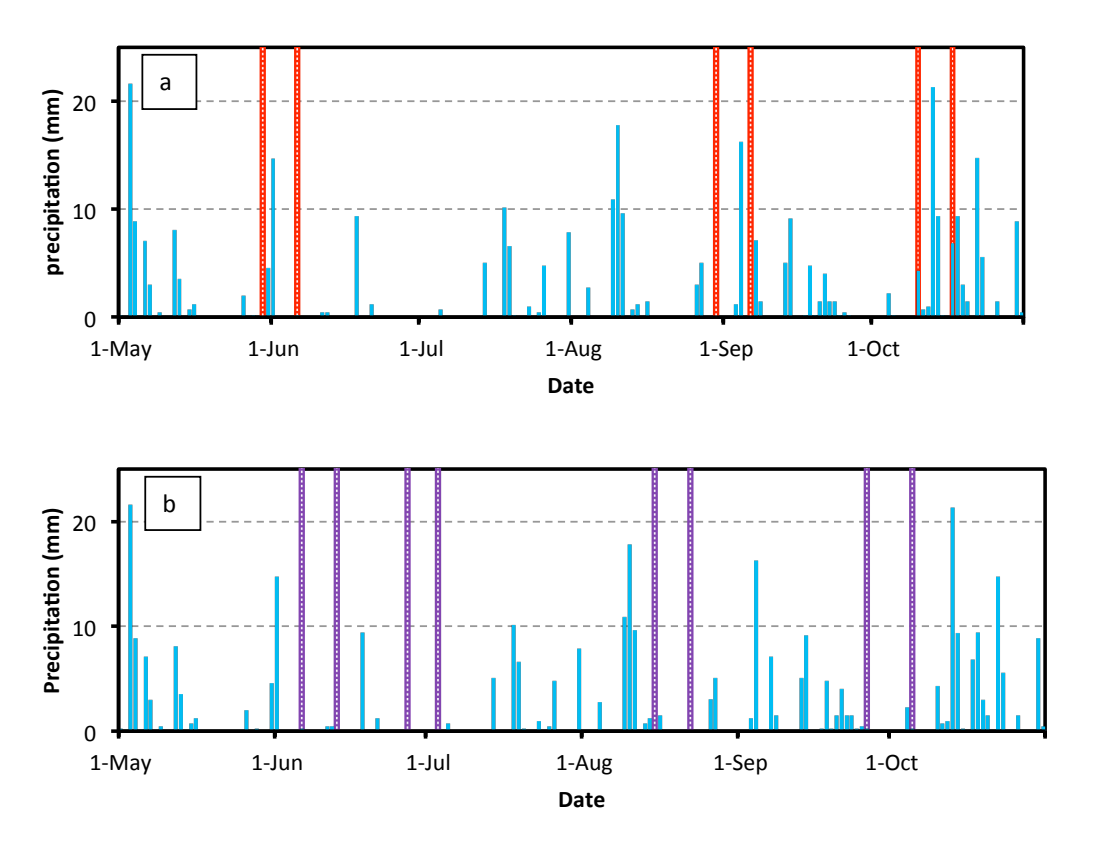


Figure 4.7: a) Weeks with high cumulative precipitation (>15 mm) in between the red lines, which coincide with ERI data collection dates. b) Weeks with low cumulative precipitation (<5 mm) in between the purple lines.

In the next paragraphs, I use contour plots to show the percent change in resistivity between consecutive periods. The images have been generated by calculating the percent difference between the (temperature corrected) resistivity inversion results for each mesh cell, $\operatorname{using}\left(\frac{\rho_{n+1}-\rho_n}{\rho_n}\right) \times 100. \text{ Here } \rho_{n+1} \text{ and } \rho_n \text{ are the resistivity values for the second and first datasets, respectively. An increase in resistivity from week one to week two will result in a positive change (yellow and red colors) whereas a decrease in resistivity will result in a negative change (blue colors).$

Figure 4.8 shows the percent change in resistivity for weeks with high cumulative precipitation (Table 4.1). Early in the growing season in early June, a week with significant rainfall did not cause a reduction in resistivity, as might have been expected (Fig. 4.8a). This shows that during the early growing season, the vegetative demand is stronger than a large input. Toward the middle to end of the growing season in early September (Fig. 4.8b) a similar amount of rain had a very different effect with a decrease in resistivity near the surface and no change at lower depth. The October event shows a strong negative response at the surface to about 0.5 m depth. A zone with very low negative values flanked by some yellows at around 19 m is likely related to the inversion process or a bad electrode, not the rain event. Other areas where the negative change extends to 1.5 and 2 m below the surface may possibly be related to areas of high throughfall.

Table 4.1: Details of cumulative precipitation during high-precipitation (> 15 mm) weeks (see Figure 4.7a for details).

Start	End	Cumulative precipitation		
Date	Date	(mm)		
5/30	6/6	19.55		
8/30	9/6	17.53		
10/10	10/17	39.56		

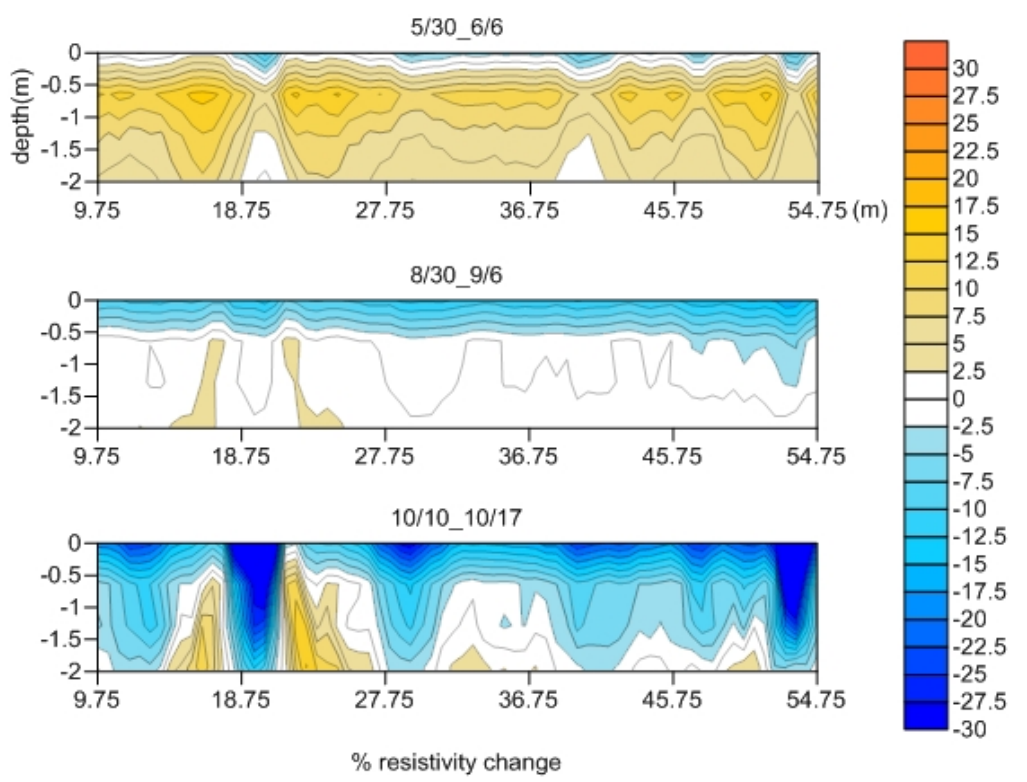
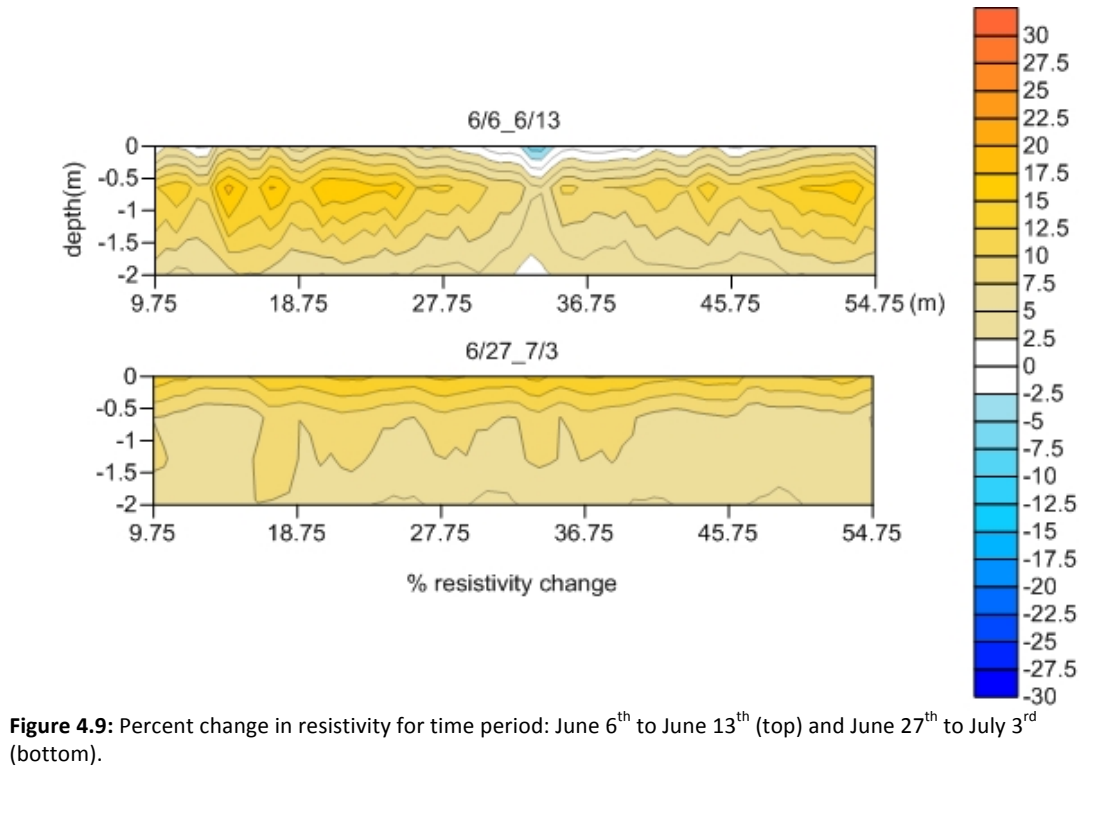


Figure 4.8: Percent change in resistivity for time period: May 30th to June 6th (top), August 30th to September 6th (middle) and October 10th to October 17th (bottom). The tick marks on the horizontal axis correspond to the boundaries of the 5 vegetation quadrats (Figure 3.1 quadrat 2 to 6)

Similar to the above, the percent change in resistivity was calculated for weeks with low cumulative precipitation (Table 4.2). The two later weeks had some bad data are not included in the analysis. The results for the two periods from the beginning of the growing season show what would be expected, which is an increase in resistivity (Figure 4.9). The week in early June shows less increase than the week in late June, even though both events had less than 1 mm of water input during that week. Although this suggests that water demands of plants increase with time during the growing season, the relationship between resistivity and water content is not linear; a correction would thus need to be applied first.

Table 4.2: Details of cumulative precipitation during low (<5 mm) precipitation weeks (see Figure 4.7b for details).

Start	End	Cumulative			
Date	Date	Precipitation (mm)			
6/6	6/13	1.01			
6/27	7/3	0			
8/15	8/22	1.53			
9/26	10/5	2.53			



Tablet period analysis

Figure 4.10 shows the time when the tablet experiments were conducted in the field. Most of them are four weeks apart, except for the third time period which lasted five weeks (for more information, refer to Table 4.3). Figure 4.11 shows the individually inverted and temperature corrected ERI data for these dates. The same inversion and plotting settings were used for all datasets. The ERI images show that the resistivity increased from early growing season in June to late September. From the end of May, there was a dry period lasting until the end of June with limited precipitation (~30 mm per month) and a relatively high air temperature (~27 °C). During this time period, the resistivity increased considerably. This increase in resistivity corresponds to a decrease in soil moisture.

After the large amount of precipitation in October, the resistivities dropped significantly.

This period coincided with lower temperatures and first leaf fall, suggesting reduced evaporative demand / vegetative needs.

Table 4.3: Details of cumulative precipitation during tablet periods (see Figure 4.10 for details).

Start	End Cumulative precipitation	
Date	Date	(mm)
5/30	6/27	31.24
6/27	7/25	24.38
7/25	8/30	65.52
8/30	9/26	55.37
9/26	10/24	81.03

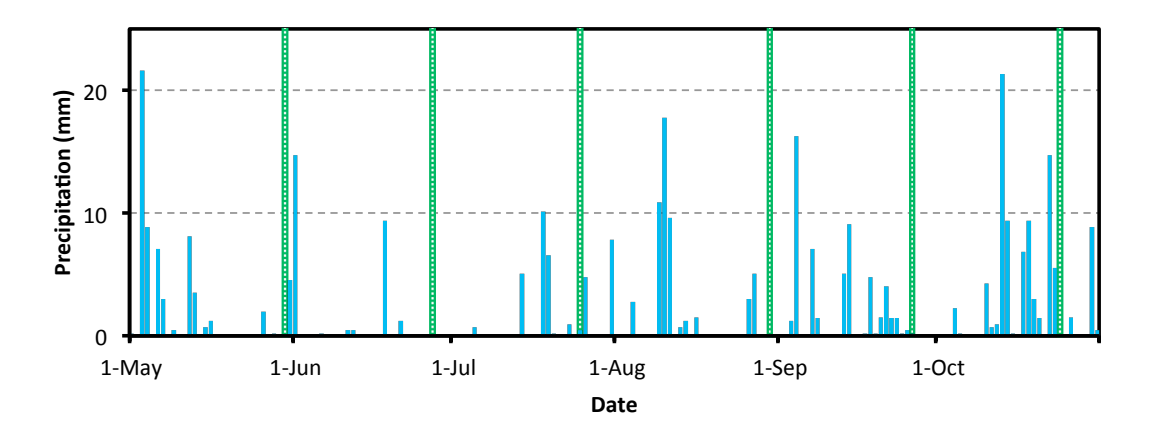


Figure 4.10: Dates of the tablet experiment (green lines) and daily precipitation throughout the study period.

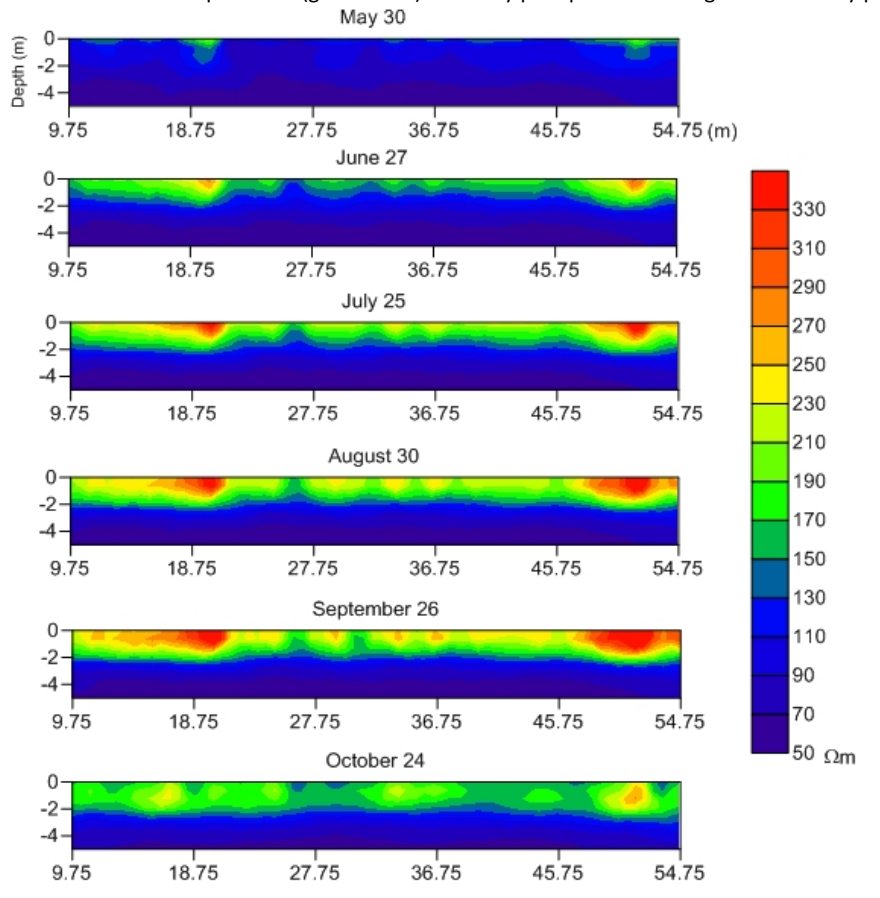


Figure 4.11: Inverted resistivity of 6 datasets that correlate with tablet swap dates.

Inverted resistivity data were converted to water contents and then plotted to show all six dates (Figure 4.12). Soil moisture decreased from the beginning of the growing season to the end of the growing season in September as water demands from plants continued. Despite the multiple rain events that occurred during the summer, soil water shows no evidence of increase for these four-week periods, which is in contrast with the wet one-week periods (e.g., Figure 4.8b). Soil water deficit only recovered after September, when plant use started to slow down and major rain events took place.

Two relatively dry (high resistivity) areas, are observed in both resistivity and the water content graphs around 18.75 m and 50 m (Figures 4.11 and 4.12). The resistivity and soil moisture plots also show some evidence of differences in spatial variability for the 5 vegetation survey quadrats and for the 6 dates. The correlation between the resistivity and soil moisture distribution with the vegetation structure will be analyzed and discussed in greater detail in the next chapter.

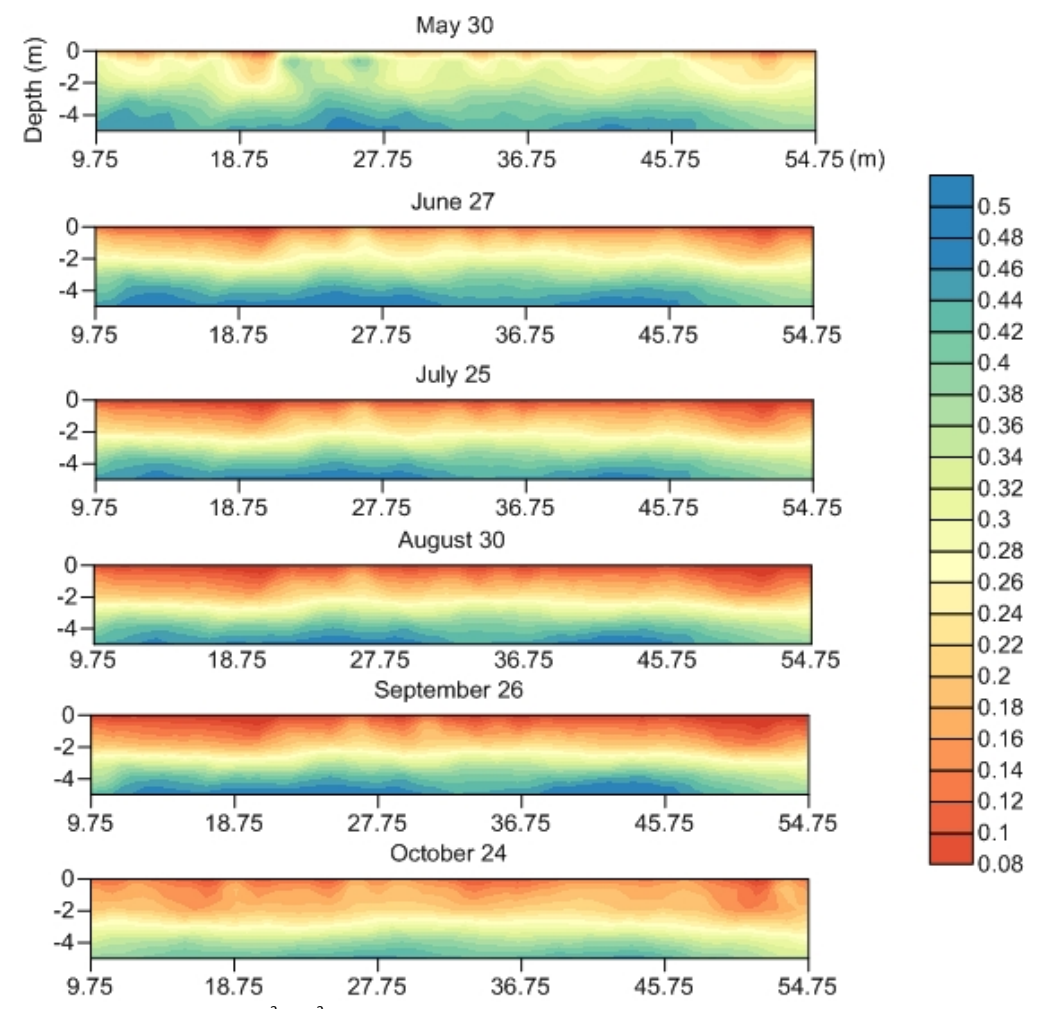


Figure 4.12: Water content (cm³/cm³) for the six dates that correlate with the tablet experiment.

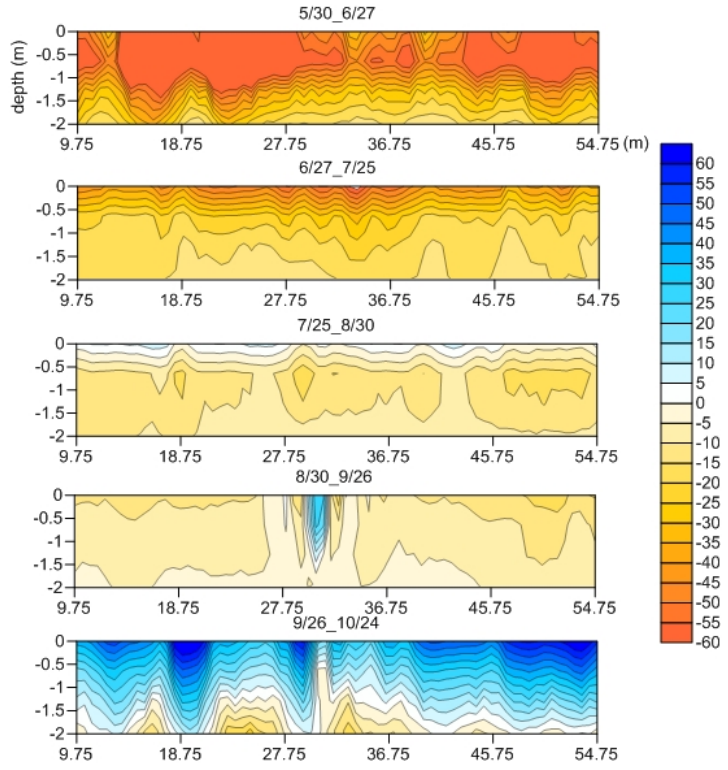


Figure 4.13: Percent difference in water content for the five tablet periods.

The difference of soil moisture between two successive tablet periods is shown in Figure 4.13. Most of the months show a negative change in soil moisture, which indicates that the water use from plants exceeds any water input from precipitation (throughfall). The series of figures shows clearly that the largest changes in soil moisture occurred early in the growing season (Figure 4.13a, b). It is possible that the lower drying for later periods (Fig 4.13c, d) reflect lower vegetative demand or the increased input of precipitation (Figure 4.10). Another possibility is that at this time when the soil is already dry, the trees take the water they need from nearby water table. This was suggested by (*Jayawickreme et al.*, 2008), who showed that the effective rooting depth of these trees extends to at least 4 m below the surface. The situation changed for the last month when air temperature dropped and plant water use

decreased. Unlike water content results (Figure 4.12), these soil moisture difference plots show no obvious relationship with vegetation distribution. Most of the changes occur near the soil surface.

Figure 4.13d shows a strong positive change in center of the study line at around 30 m. The dimension of this anomaly is around 0.5 m wide and 1.5 m deep. In the meantime, Figure 4.13e shows a positive change at the same spot. Given the vegetation structure of the site and water content graphs, there is no link to root distribution. The reason to form this kind shape is probably related to a bad data point around 30 m in the September 26th file. A differential inversion could possibly fix this problem.

Climate variables

Throughfall from tipping bucket data

Based on the precipitation record from the forest side tipping bucket, real time rainfall was tabulated. Any break in the rainfall record for one hour or more, resulted in separate rain events before and after that interval. The tabulation was used to calculate the duration of each event (hours) and the total amount of rainfall (mm), which is also called precipitation depth.

This allowed calculation of rainfall intensity (mm/hr) for each event. The duration of each rainfall event and the calculated intensities were improved from MAWN data (1-hour maximum resolution) by using the actual durations as observed using the tipping bucket rain gauges at the field site. Figure 4.14 is a plot of duration versus precipitation depth for each event. Among all 53 identifiable events, most of them have both low depth and short duration. However, there are a few events with long duration (> 12 hours) and/or high precipitation depth (>15 mm).

Figure 4.15 shows the relation between rain intensity and duration for the same 53 events as in Figure 4.14. It shows that most of the events have low intensity irrespective of the duration. All long duration events had a low intensity.

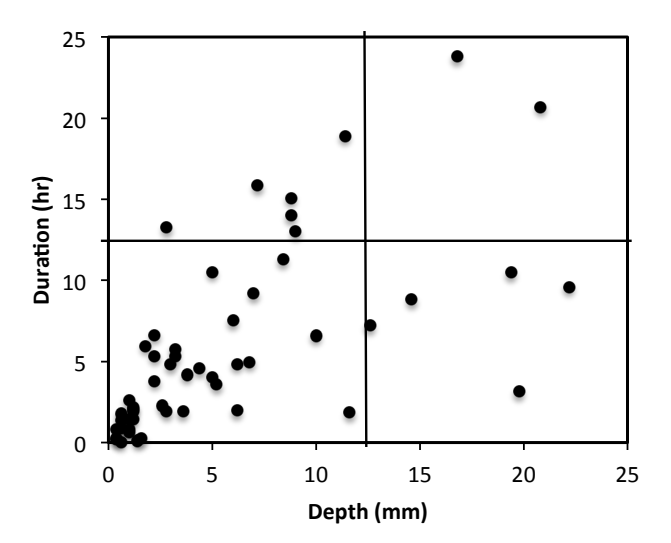


Figure 4.14: Rain event characterization based on MAWN hourly precipitation data.

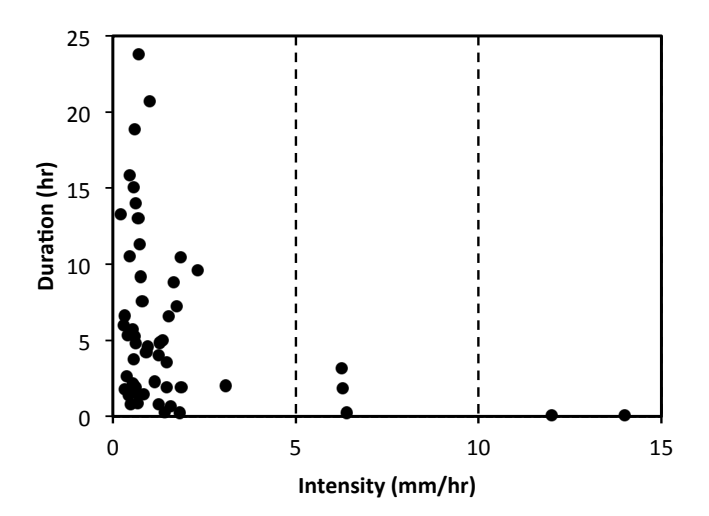


Figure 4.15: Rain intensity (mm/hr) compared with duration (hr).

The rain gauge in the grassland was set up to measure rainfall without interception, whereas the forest gauge measured throughfall not intercepted by the canopy. Therefore, the difference in measurements between the two gauges should be equal to the interception (including stemflow) losses. Comparison between the throughfall collected at the forest side and the open-field precipitation at the grassland side is established based on 14 events from July and October. As discussed before, high intensity events were rare during the growing season of 2012, and most events had less than 10 mm of rainfall. The least-squares regression line is shown in Table 4.4.

The results of the comparison between the forest and grassland bucket (Figure 4.16) show that the throughfall fraction of the forest is on average 1/1.2565 = 0.8. There is no clear indication that the throughfall fraction varies with rainfall depth. However, most events from 1 to10 mm (grassland tipping bucket) fall above the trendline, suggesting that for these low depth events, the throughfall fraction is slightly lower than 0.8.

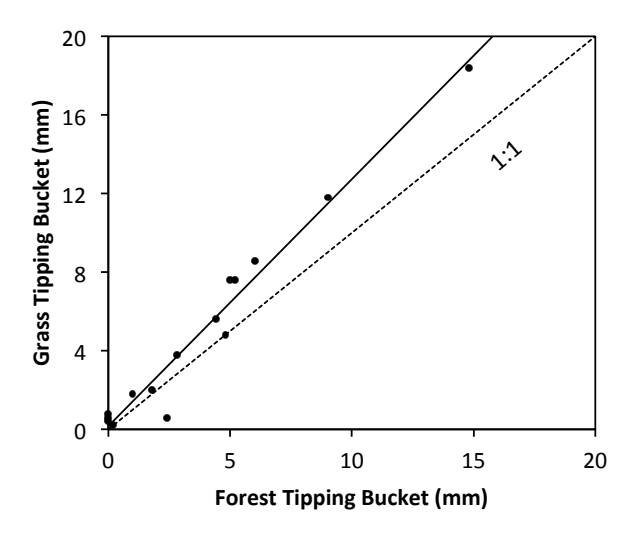


Figure 4.16: Relationship between data collected in the forest and grassland.

Table 4.4: Coefficients and related data for linear regression models fitted to throughfall and precipitation data

Relation	Intercept (a)	Coefficient (b)	Coefficient of determination (r ²)	Standard error of estimate
Tipping bucket rain gauge record (mm): forest vs grassland	0.1652	1.2565	0.9657	0.7868

Throughfall from TIFs

To assess the quality of the data, a graph has been made to compare the fractional weight loss for each table period in the forest and grassland. The weight loss fraction is obtained from $\frac{m_{before}-m_{after}}{m_{before}} \times 100$, where m_{before} and m_{after} are the tablet weights before and after use in the field. The funnels in the forest were divided into two types (for details see Figure 3.1):

- a) All 18 funnels in the forest ("forest_all), which included the 3 random funnels (#22-24) and all 15 funnels co-located with electrodes and vegetation quadrats 1-7 (#1-15), and
- b) The 11 funnels (#3-13) co-located with electrodes and vegetation quadrats 2-6 ("forest_selected").

The tablets for the funnels in the grass have a higher weight loss since these funnels record all precipitation while for funnels in the forest some rainfall has been intercepted. The difference between the fractional weight loss for the Forest_select and Forest_all groups is very small (Figure 4.17).

Data analysis of the throughfall integrating funnels shows a strong positive correlation between average weight loss and cumulative precipitation recorded at the MAWN site (Figure 4.17). The best fit regression lines approach the origin of the graph, suggesting a linear relationship between precipitation amount and weight loss, unrelated to the dominant type of event during each period. Figure 4.17 also clearly demonstrates that the forest TIFs have a smaller weight loss the open-field TIFs, as was expected. There is no evidence for a change in throughfall fraction for relatively wet versus dry months. The strong positive correlation shows the quality of these measurements.

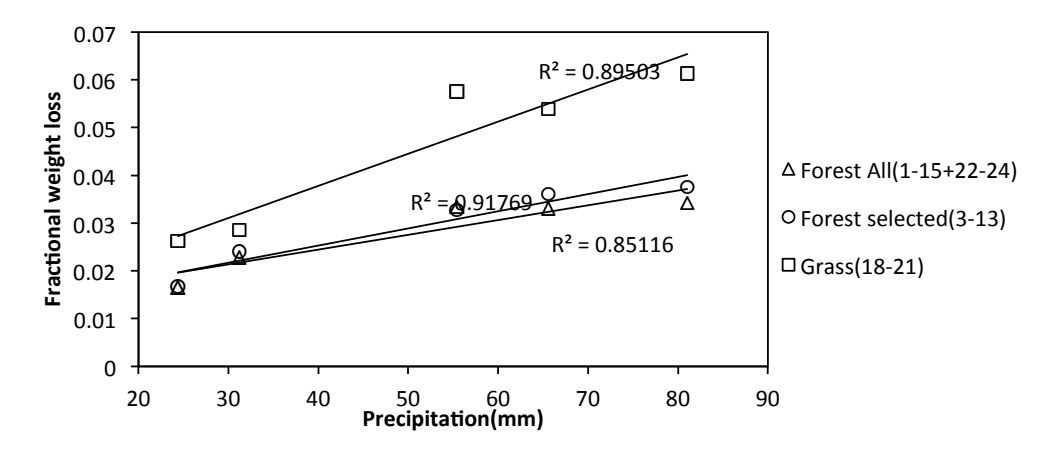


Figure 4.17: Cross plot of cumulative weight loss versus precipitation for five periods of appoximately four weeks. The lower weight loss fraction in the forest shows the effect of throughfall.

Chapter 5 Discussion and Conclusion

In this chapter, I will discuss the results from last chapter and will address the main objectives of this thesis, which are to study whether the spatial pattern of soil water remains the same during growing season and whether spatial variability of soil water is correlated to vegetation structure and throughfall.

Regarding the second objective, the results in the previous chapter suggested that such a relationship exists as areas of high resistivity seem correlated with areas with densest vegetation. For an example of this, see Figure 5.1, which shows the correlation between vegetation distribution and the resistivity profile of September 26th. In this chapter, I will discuss soil moisture, soil temperature and throughfall spatially and temporally with the vegetation distribution as background.

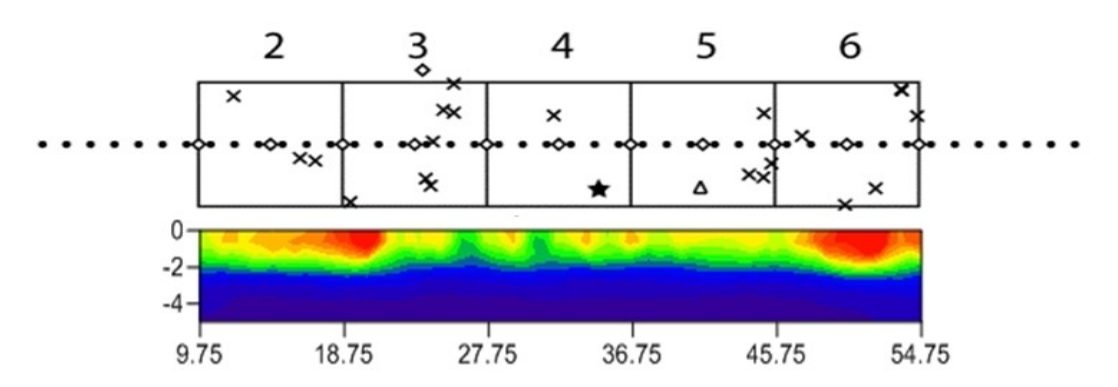


Figure 5.1: Tree survey quadrat along with September 26 resistivity profile (Color scale see Figure 4.11).

To begin this chapter, I will first show the results from the vegetation survey obtained from the field. Then, I will analyze soil moisture and throughfall spatially and temporally.

Spatial analysis of vegetation parameters

Vegetation structure and LAI

The tree survey shows that along the measurement line there are two distinct areas with a clustering of trees(Figure 5.2). These clusters are separated by an approximately 15 m wide area with low tree density in the middle of the forest (27 - 42 m).

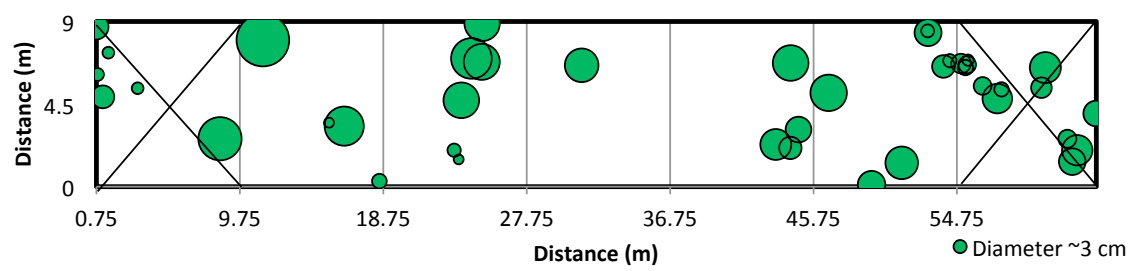


Figure 5.2: A tree survey shows locations of trees and scaled diameters at breast height. Vegetation quadrat 1 and 7 were not included in the analysis (See Figure 3.1 for sensor locations).

Due to the difficulty of measuring crown height and tree height quantitatively during the vegetation survey, qualitative observations of those parameters were made in June 2013.

Additional variables measured in the qualitative survey include crown depth and tree living condition. I estimated the average height of the trees at about 25 m, but there is considerable variability, related to age and crown conditions. Full details of the vegetation survey are given in Chapter 3 and Appendix B. Trees at the site have various shape of canopy based their living condition and solar availability.

The results show that there are slightly more tall trees than short trees at site (Figure 5.3). Most of the trees are alive at the time we surveyed the site, however, there are few dead trees as well but the time when they died is unknown. Overall, the majority of trees have

relatively narrow crowns. There is an approximately equal division between trees with deep and shallow canopies.

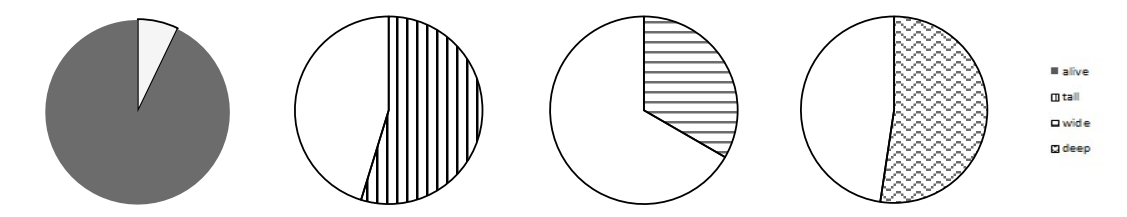


Figure 5.3: Pie chart of the qualitative tree survey.

A bar graph is created for each vegetation quadrat including all the variables mentioned above (Figure 5.4). For each quadrat, this graph shows the total numbers of trees, the number of alive and tall trees, and the number of trees with wide and deep canopies. It shows that vegetation block 3 and 6 have the most alive individuals, but quadrat 6 has more tall and deep crown trees than quadrat 3.

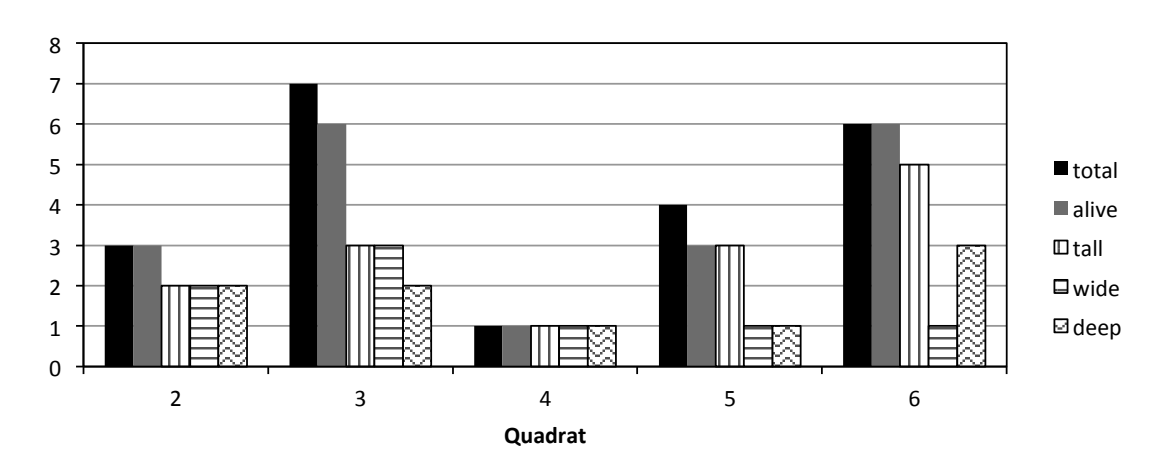


Figure 5.4: Bar graph for each vegetation quadrat with results of the vegetation survey.

Leaf Area Index (LAI) was measured once during the study period in September 2012.

LAI results are shown in Figure 5.5 and are compared with the estimated crown area for vegetation quadrats 2 - 6 (data for individual trees in Appendix B). The LAI and estimated crown

areas show a good correlation with highs in vegetation survey quadrats 2 and 6 and a distinct low for vegetation survey quadrat 3. The low in quadrat 3 is surprising as this quadrat has the largest number of trees and it has a similar number of trees with wide and deep crowns as the other survey quadrats. Based on tree density distribution (Figure 5.2), the first vegetation cluster ends around 27 m with an approximately 15 m wide area with low tree density in between the two vegetation groups. The lowest LAI values being observed in quadrat 3 instead of quadrat 4 could relate to the angle of sunlight. LAI was measured in the morning during a sunny day, with sun rays entering the forest from the southern edge. Also, LAI at 9.75 m is relatively low. This is probably related to vegetation quadrat 1 (see Figure 5.2), where six trees are observed. This could also relate to the sunlight, which created extra light on the other side of the forest.

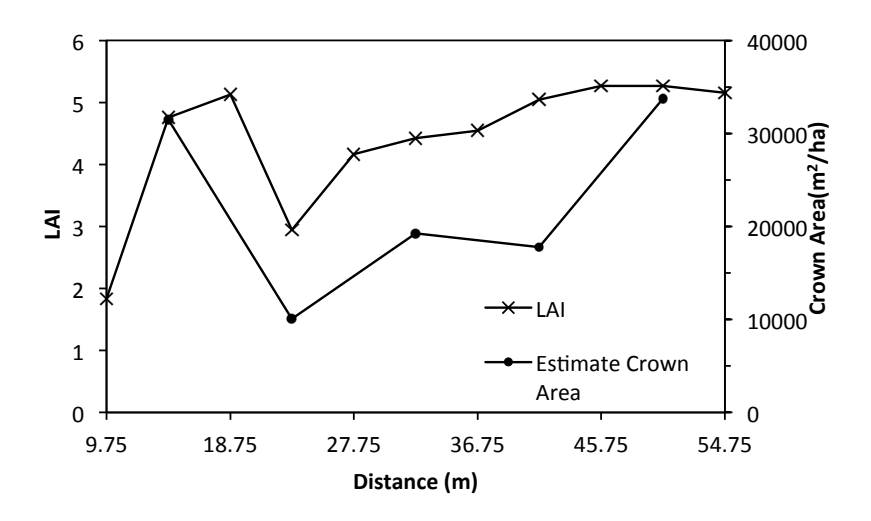


Figure 5.5: LAI measurement result and estimated crown area for vegetation quadrats 2-6.

Similar to the above, a plot that compares number of trees in each quadrat and the basal area is generated (Figure 5.6). It shows that quadrat 2 has only three alive trees. However,

the basal area is the highest, which indicates big trees are observed in this vegetation quadrat. Besides quadrat 2, quadrat 3 to 5 have a good correlation between tree basal area and number of trees. Quadrat 4 (in between 27.75 m and 36.75 m) has the least amount of both trees and smallest basal area. Quadrat 6, which is closer to the forest edge, has high number of trees yet the basal area is relatively small.

The vegetation survey as it has been conducted has some limitations. The primary issue is the relatively small vegetation quadrats of 9×9 m. Another potential issue is the timing and conditions of the LAI survey, with sunlight entering the forest from the southern edge possibly affecting the readings.

Combining all information I believe that the densest canopy along the line is around 9.75 m to 54.75 m based on crown area and LAI information. However, quadrat 3 has the largest basal area with low canopy coverage.

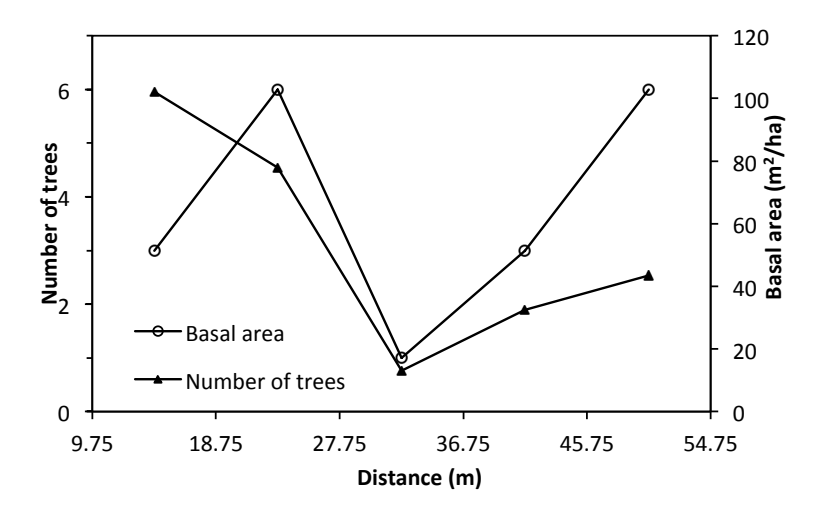


Figure 5.6: Tree basal area and number of trees in vegetation quadrats 2-6.

Several areas of increased wetting after each high precipitation period are identified based on percent change in soil moisture near the surface. The data in Figure 4.8a and Figure

4.8c suggest that the spatial distribution of wetting patterns are consistent for different high rainfall periods (identified using six red dashed lines in Figure 5.7a), which may be due to spatial heterogeneity in canopy coverage or other vegetation variables. To further investigate the dynamics of soil wetting behavior at the site, I profiled the percent change in water content along the line for the three high-rainfall periods in Figure 5.7b. For this, I plotted the surface water content change at 0 cm depth at each electrode location. High precipitation week October 10th to 17th received almost twice as much rainfall as the other two weeks. Thus, the wetting behavior for that week is most obvious. The high change area within quadrat 2 could be related to fewer number of trees at the border of quadrat 2 and 3 (Figure 5.2). Similarly, the identified high change areas within quadrat 3 to 5 could be related to low LAI (Figure 5.5). High number of trees or low LAI would cause strong wetting during high precipitation periods. As expected, the six wetting areas shown in the resistivity plot (Fig. 5.7a) are comparable to the water content profile for all three of the high precipitation periods (Figure 5.7b).

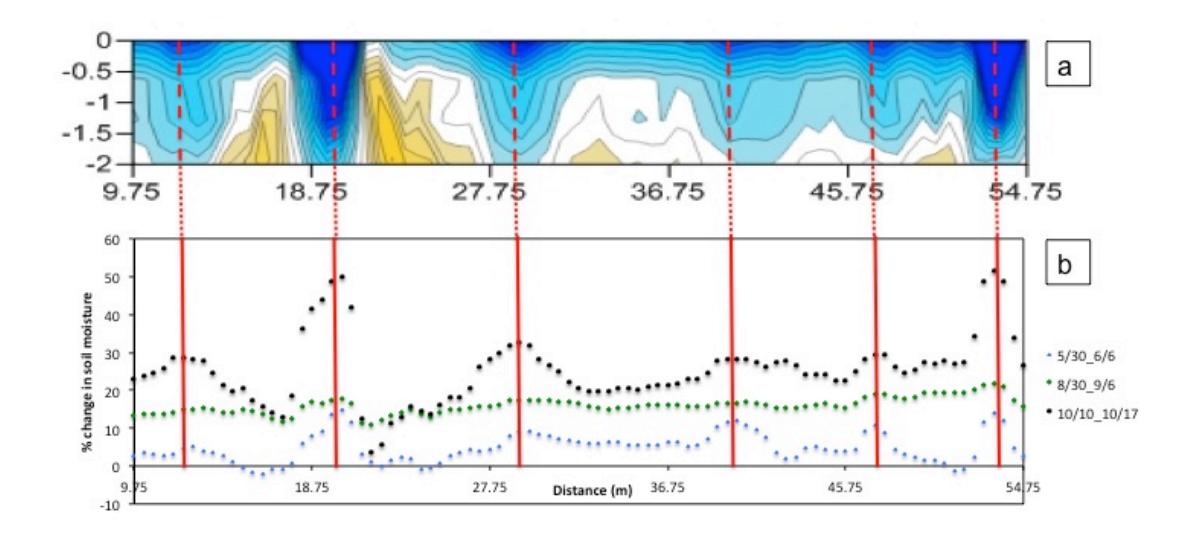


Figure 5.7: a) Six areas of strong negative resistivity changes for the high-precipitation week from October 10th to 17th. b) Percent change in soil moisture along the transect for three high-precipitation weeks (Table 4.1). Solid red lines correspond to the areas of high negative resistivity change area in (a).

Spatial and temporal analysis of soil dynamics

Soil moisture and soil moisture changes

To acquire insights on the spatial distribution of soil moisture and to enable comparison with the vegetation structure, the average soil moisture for each of the vegetation survey quadrats was calculated. This calculation was performed for each of the six tablet swap dates. The results are plotted for three different depth ranges (0–50 cm, 50–100 cm and 100–200 cm) to emphasize different parts of the root zone (Figure 5.8). The results show that first data set on May 30th had the highest soil moisture among all six dates, irrespective of the depth. Lowest soil moisture is observed in between 0 and 50 cm throughout the growing season, this could relate to high air temperature and active vegetative use which dries the surface soils. Soil

moisture distribution is fairly constant across the array for different depths. A decrease in soil moisture is observed for vegetation survey quadrat 6 for most depths and times.

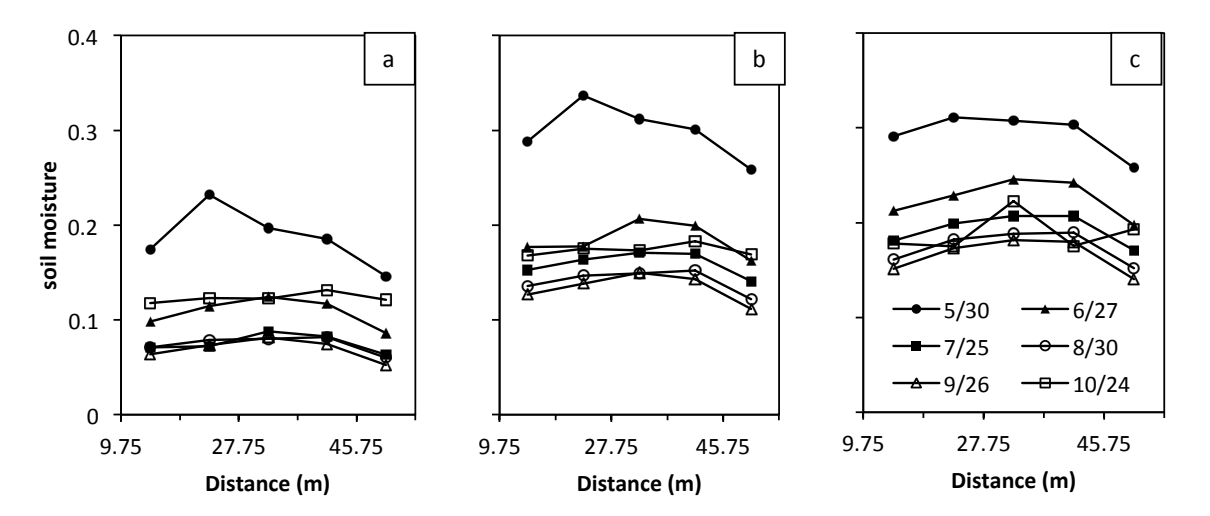


Figure 5.8: Average ERI-derived soil moisture for vegetation survey quadrats 2-6 integrated over a) 0-50 cm, b) 50-100 cm, and c) 100-200 cm depth. Data points are plotted at a horizontal distance representing the middle of each vegetation quadrat; the tick marks represent the edges of the vegetation quadrats.

The soil moisture difference between tablet periods is shown in Figure 5.9. The results show that for most of the tablet periods the soil moisture change is negative, except for October at all depths. The percent change that involves May 30th shows a significant negative change in soil moisture. Given the moisture of that date is around 0.3 (Figure 5.8 b,c), this negative change represents natural but significant drying. The 0-50 cm depth seems to show the most variations in soil moisture changes. Most of the changes are negative and are around 20%, this means no matter how much precipitation input during that four week period, soil moisture was always inadequate. The smallest changes always occur in between 27.75 and 36.75 m (vegetation quadrat 4), which had the fewest amount of trees and smallest basal area. This is probably related to the soil rather than interception. If it's related to interception, quadrat 4 should have the high moisture changes because quadrat receives the highest through.

However, the results show the opposite. Given that growing season 2012 received only 257 mm rainfall in total and it had 84 days with temperature higher than 25°C between May 30th and October 24th, I think that soil at quadrat 4 dried out and wetted up less than the other quadrats with high canopy coverage and high vegetative root water uptake.

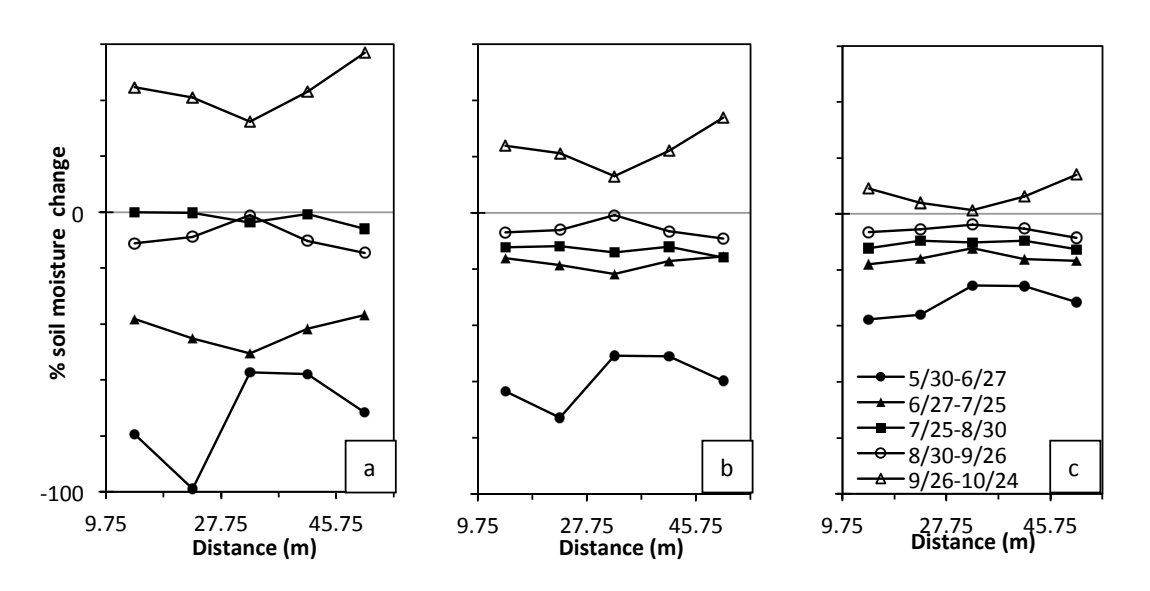


Figure 5.9: Percent change in soil moisture between table period for vegetation survey quadrats 2-6 (9.75 m to 54.75 m) integrated over a) 0-50 cm, b) 50-100 cm, and c) 100-200 cm depth.

Soil temperature

Soil temperature acquired from temperature ibuttons at 5 cm depth below ground was analyzed by calculating the average temperature for each of the tablet periods and the entire growing season survey period. The results are plotted in Figure 5.10 and show the seasonal trend of the subsurface temperature. Temperature at 5 cm depth varied from 7 to 22°C during growing season. The average of the whole study period is around 17°C. Changes in temperature are quite subtle based on the results. There is a temperature low around 9.75 m, which could be caused by a slightly deeper installation or by some shade created by nearby shrub, for

instance. The slightly lower temperatures between 18.75 m and 27.75 m (vegetation survey quadrat 2) are probably related to dense tree presence (see vegetation structure in Figure 5.2). The drop-off by the forest edge is shown in all periods, possibly due to the high tree density and lower light input. The high LAI that extends over a relatively wide area (Figure 5.5) supports this theory.

My approach of performing the temperature correction of ERI data in Chapter 4 did not take temperature spatial variability into consideration. Based on the spatial temperature ibutton results presented here, this assumption is acceptable. In Chapter 4, spatial variability in resistivity and soil moisture are observed. Figure 5.10 helps to eliminate the possibility that the spatial variability of soil moisture is caused by temperature.

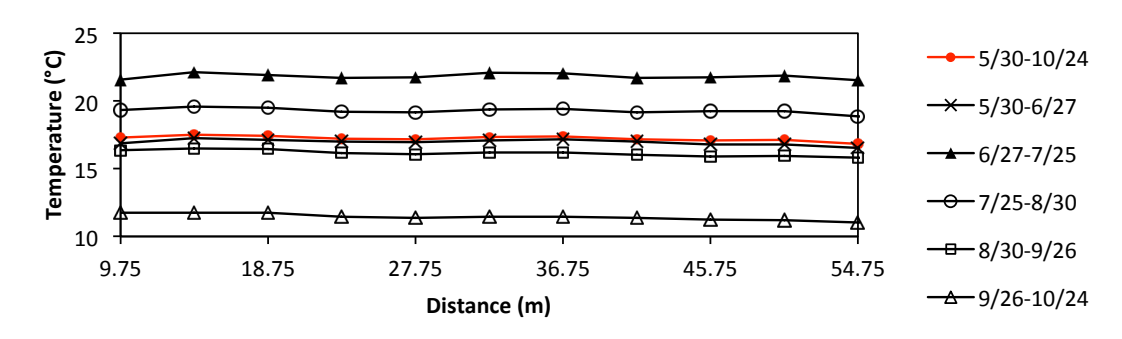


Figure 5.10: Average temperature obtained from bi-hourly ibutton temperature readings for the whole study period (red) and five tablet periods.

Geostatistical analysis

Average inverted resistivity at 25 cm depth is calculated for 91 data points from 9.75 m to 54.75 m and plotted below in Figure 5.11. During the growing season, a steady increase of resistivity is observed from late May to late July. After that, resistivity stayed in between $200\Omega \cdot m$ to $250\Omega \cdot m$ until late October.

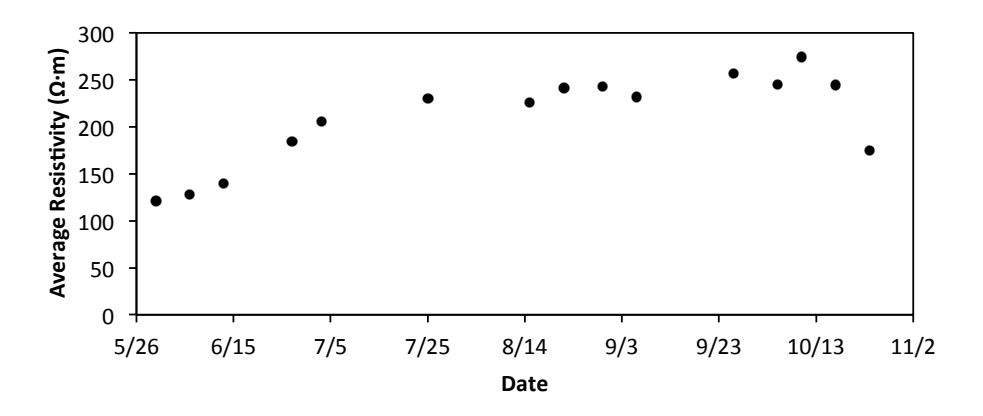


Figure 5.11: Average electrical resistivity (after temperature correction) throughout the growing season.

To analyze the data statistically, 131 resistivity data points at 25 cm depth were used to generate the variograms. This covered the entire inversion mesh, not just vegetation quadrats 2 to 6. There are three major components in each variogram: the sill, the range (correlation length) and the nugget. If the sill exists, the semivariance flattens at that level. The sill can be viewed as the spatial variance between two remotely distributed points (*Western et al.*, 1998). The range is the distance at which the variogram reaches its sill and the nugget is the vertical jump from 0 at the origin to the value of variogram at extremely small separation distance, due to small scale variability or sampling error. A spherical model was used for all six variograms (Figure 5.12). The sill has a wide range from 500 to around 4000. The nugget value varies from 0 to 50.

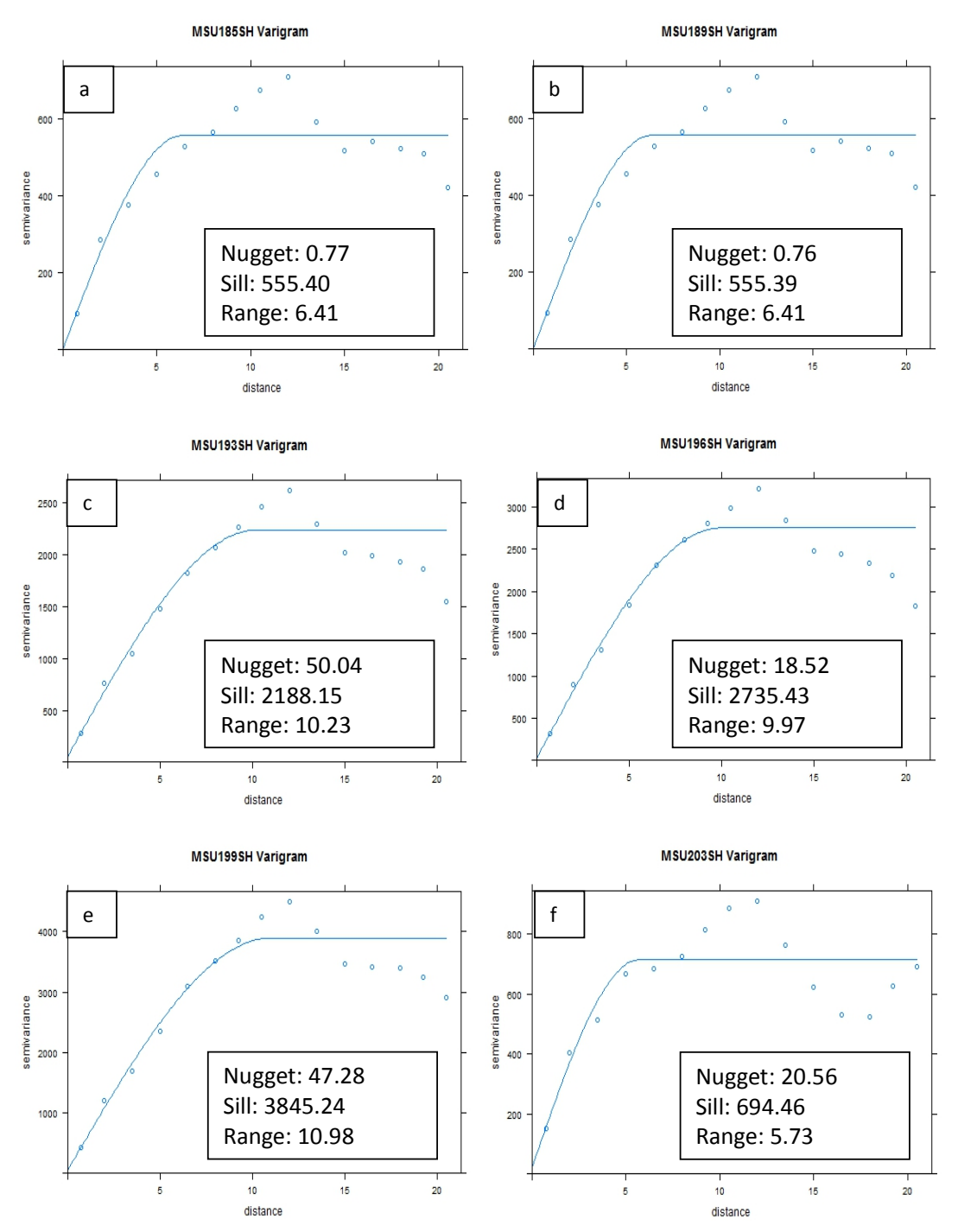
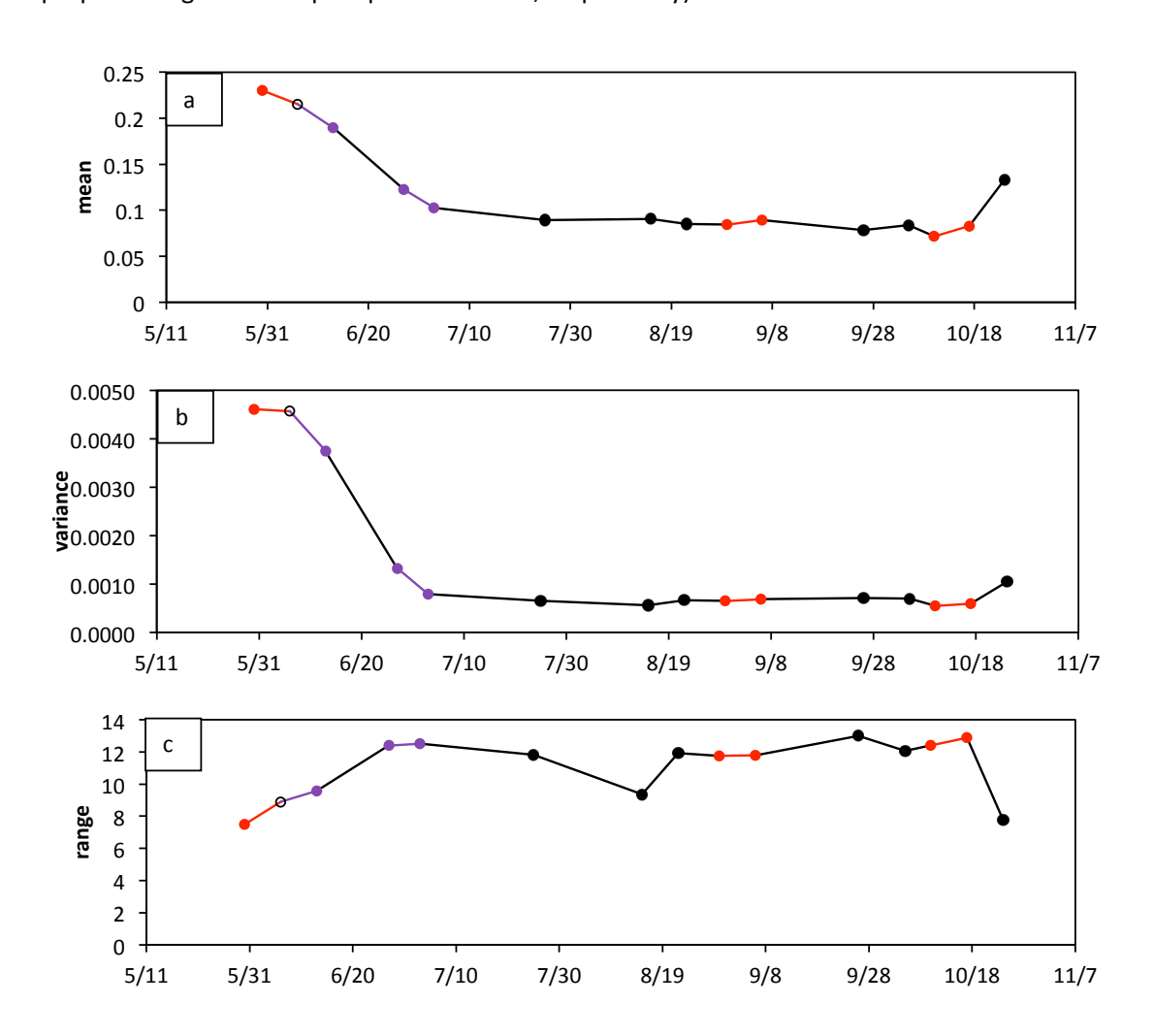


Figure 5.12: Geostatistical analysis on first layer of the resistivity data of six dates that correlate with the tablets replacement dates a) May 30, b) June 27, c) July 25, d) August 30, e) September 26, and f) October 24.

Water content was obtained from the temperature corrected resistivity data (see Fig 4.12). Here, I will discuss the spatial and temporal changes of soil moisture near the soil surface. Changes of soil moisture of the first 50 cm are shown in Figure 5.8a and the evolution of the geostatistical structure is shown in Figure 5.13 using the same color code as in Fig. 4.7 (red and purple for high and low precipitation weeks, respectively).



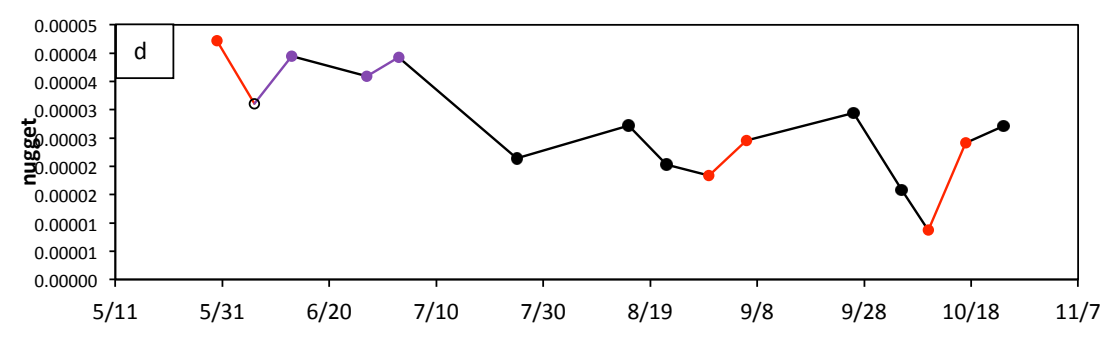


Figure 5.13: Temporal evolution of the geostatistical structure of the soil moisture pattern at site, for the datasets previously analyzed. a) mean soil moisture, b) spatial variance, c) range and d) nugget. Red and purple colors are used to highlight high and low precipitation weeks, respectively (see Tables 4.1 and 4.2).

The spatial variance (sill) changes between 0.001 and 0.045 with a seasonal trend. Since sill is measuring two remotely distributed points, small sill would indicate relatively uniform soil moisture. In the soil moisture graph, among the six selected dates, early June and late October seem to have the most obvious changes in soil moisture. This trend is determined by the mean soil moisture tendency.

The ranges vary between 7 and 13 and it's showing some difference between the wet periods and the dry periods. The ranges of the wet periods seem to be a little bit lower than the dry periods overall. Similar to the spatial variance, this is also related to mean soil moisture but the trend is the opposite.

The nugget fluctuates between 1 and 4. The changes of nugget don't have the consistency as either the sill or the range. The overall tendency of nuggets between dry and wet periods isn't very obvious. However, the variation of the nugget does seem to be a lot smaller than the variation of the sill.

Both the mean and variance graph show a similarity throughout of the growing season.

Both variables decreased as soil moisture decreased at early growing season and increased

when soil moisture deficit recovered closer to the end of the growing season. There is no clear correlation in between dry and wet periods.

Spatial and temporal analysis of throughfall

Dunkerley (2010) validated the method using *plaster of paris* tablets to measure throughfall. Figure 4.18 confirmed that these throughfall integrating funnels (TIFs) are also valid for this particular research. The average weight loss for each funnel along the survey line is plotted in Figure 5.14.

In vegetation quadrat 2 and 3, which have the densest canopy coverage and largest basal area, respectively, the weight loss fraction is relatively low. This indicates that a big portion of rainfall was intercepted by the canopy for this survey quadrat. Between 45.75 m to 54.75 m (vegetation survey quadrat 6), a low weight loss fraction correlates with the high LAI (Figure 5.5). Within quadrat 4, where the basal area and number of trees was very low (Figure 5.10), the weight loss fraction is relatively high, but only for some locations and tablet periods. The low weight loss at gird 3 could be potentially related to stemflow.

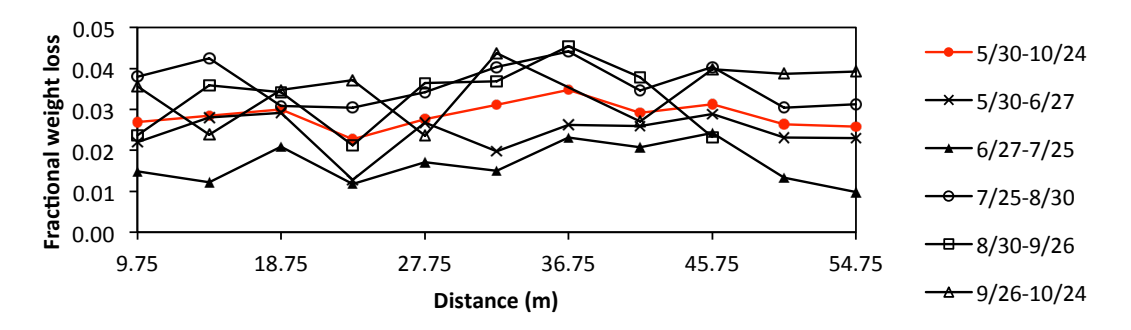


Figure 5.14: Tablet fractional weight loss for each of the TIF locations along the survey transect in the forest. The tick marks represent the edges of the vegetation quadrats.

Throughfall depth (mm) was calculated using averaged fractional weight loss and weight loss coefficient. The monthly weight loss coefficient (% change in tablet weight per mm rainfall) was obtained from the grass tablets fractional weight loss (%g) and monthly cumulative

precipitation (mm). In this case, I assume that tablets weight loss in the open field is solely dependent on cumulative precipitation (no interception). Fractional weight loss at forest locations is then converted to throughfall depth using data collected for the entire study period. Figure 5.14 shows the throughfall depth trend along the transect. Vegetation quadrat 3 has the least amount of throughfall, which is acceptable because gird 3 has more trees than the other quadrats. Also, the relatively high throughfall in quadrat 4 and 5 and low value at quadrat 3 and 6 agree with most of the soil moisture distribution (Figure 5.8). However, according to Figure 5.5, some of the behavior of throughfall depth is more difficult to explain. This could be related to the limited LAI data.

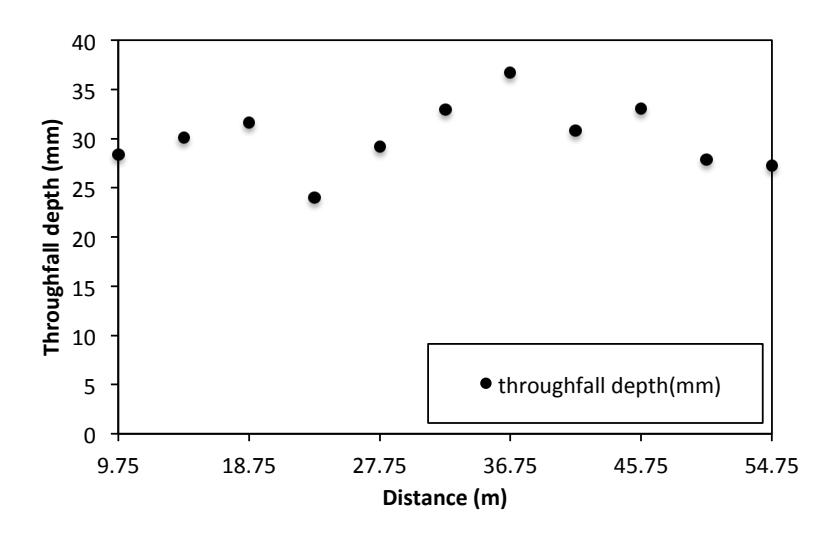


Figure 5.15: Throughfall depth calculated from tablet weight loss fraction.

Quantitative Comparisons

To quantitatively compare soil parameters with vegetation structure and throughfall, I compared (a) soil temperature and soil moisture, (b) soil temperature and different vegetation characteristics, (c) soil moisture change and tablet weight loss and (d) soil moisture and

vegetation characteristics. Temperature was normalized to 0 to 1 scale, where 0 and 1 are the minimum and maximum temperature for a time period. Similarly, tablet weight loss were normalized to correct for different starting weights of the tables and scaled to 28-day periods. Soil moisture was averaged for each quadrat at 0-50 cm.

The correlation between soil temperature (both absolute and differenced between data collection periods) and vegetation parameters and soil moisture did not produce statistically significant correlations (Figure 5.15 and 5.16). This was an expected result based on the earlier observation of limited spatial variability in soil temperature along the transect. During the first two months of the growing season the soil dried relatively fast, especially in the shallow soil layers (Figure 5.9a).

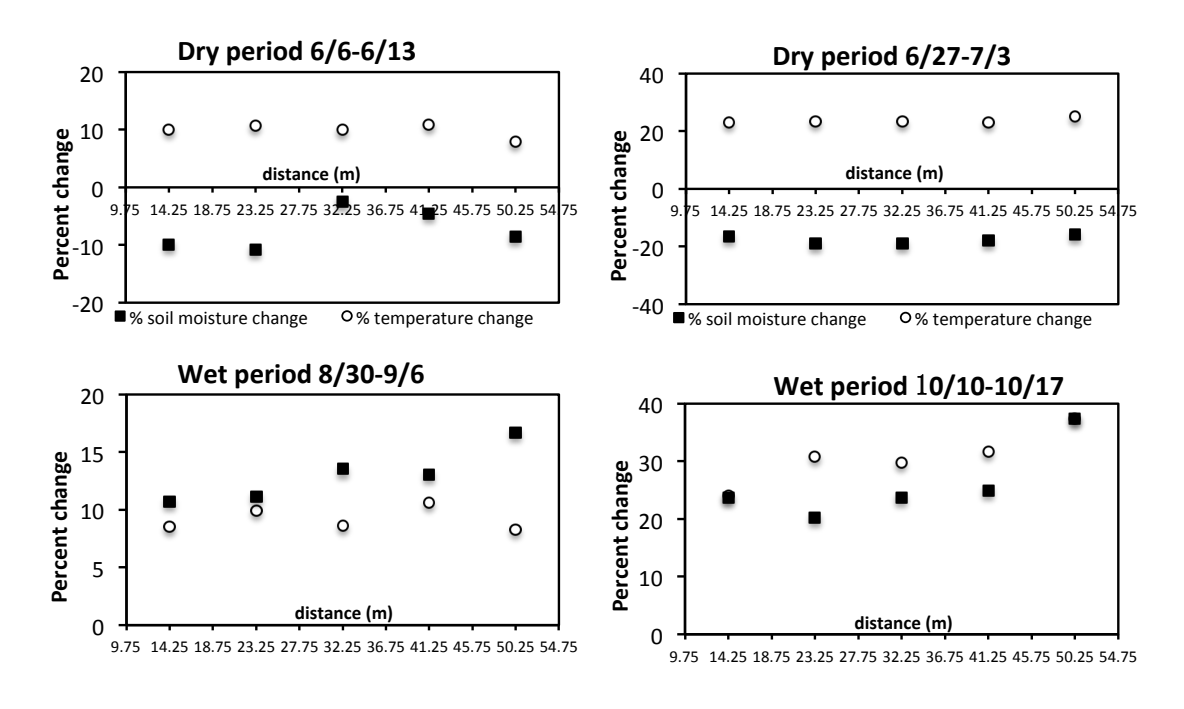


Figure 5.16: Comparisons between percent change in soil temperature and soil moisture for dry and wet periods.

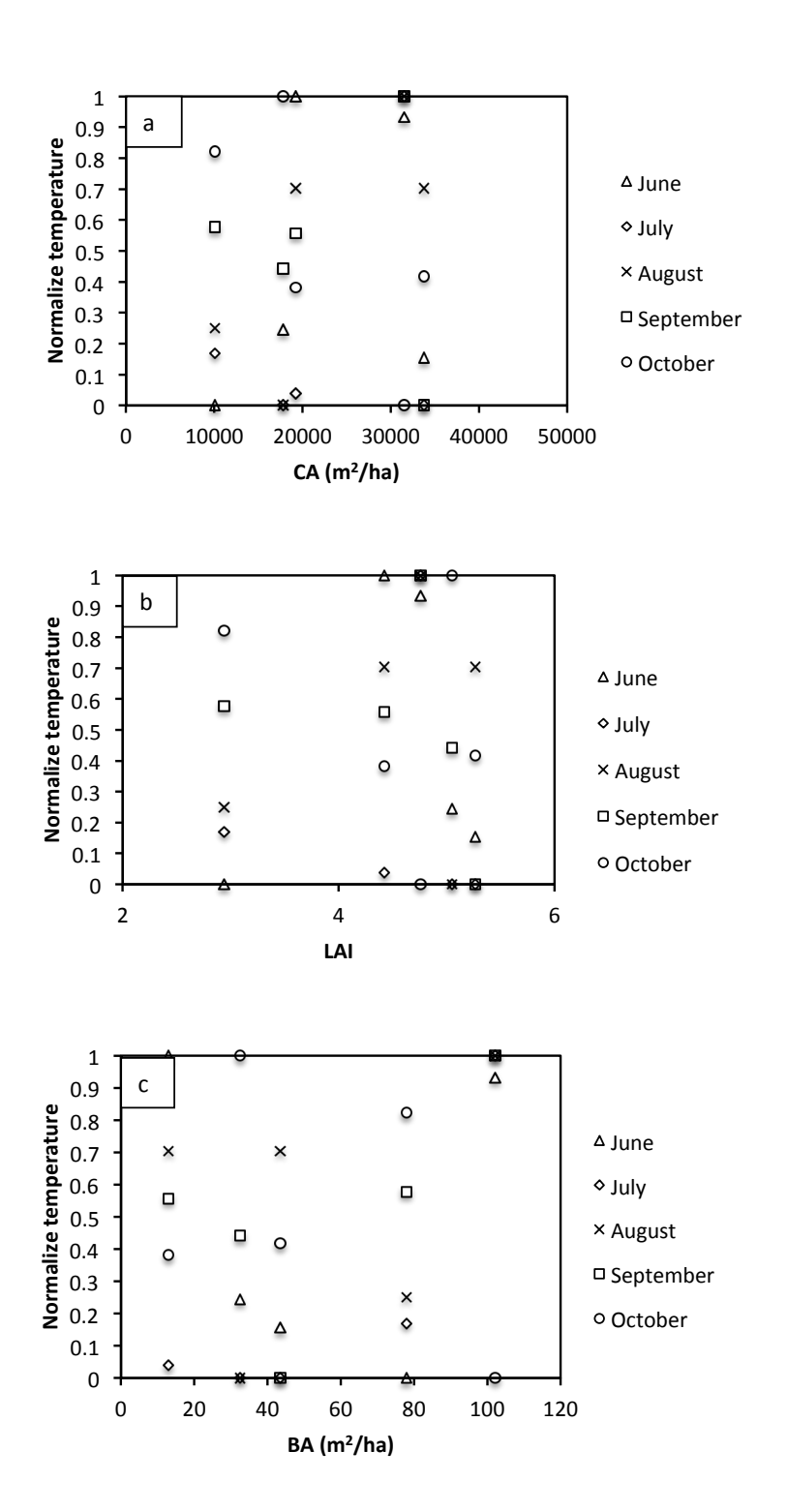


Figure 5.17: Comparisons between soil temperature and a) crown area, b) LAI and c) basal area.

A comparison of soil moisture change and normalized tablet weight loss for these months show that in quadrats with more throughfall, the drying is less pronounced (Figure 5.18). This result is as expected, but the correlations are weak. This may be the result of the previously discussed strong heterogeneity in throughfall that is difficult to capture using the TIF method and limited measurement locations. During the third and fourth tablet periods, when soil moisture content changes relatively little (Figure 5.9), there is no correlation between tablet weight loss and the soil moisture change (Figure 5.19). During the final tablet period, strongest wetting is concentrated in quadrats with less throughfall. This result may indicate that in these quadrats the growing season moisture deficit was most significant.

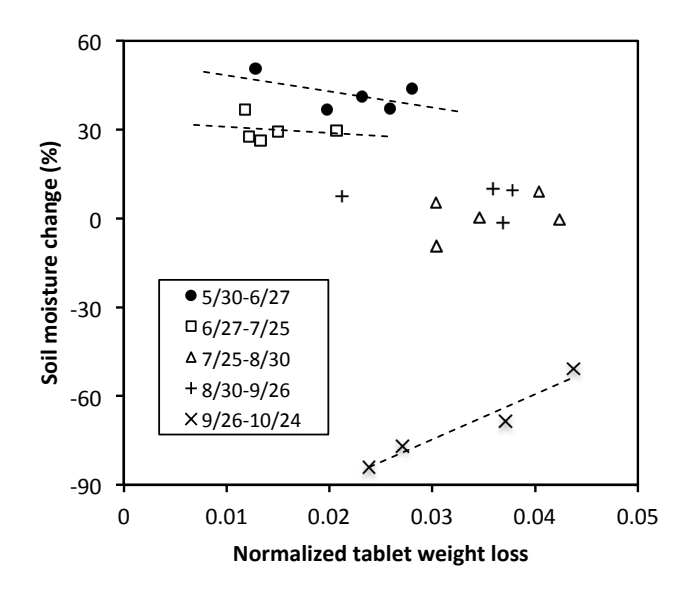


Figure 5.18: Comparison between soil moisture change and normalized tablet weight loss. Linear regression lines are given for datasets on May-June, June-July and September-October periods.

A quantitative comparison between soil moisture and vegetation characteristics shows a strong negative correlation with crown area (Figure 5.19) and LAI during the growing season.

This correlation between soil moisture and canopy indicators was strongest at the start of

growing season, when quadrats with more canopy (high LAI or large crown area) had distinctly lower soil moisture contents. The slope of this correlation gradually dropped throughout the growing season (although the correlation coefficients remain strong), which suggests that the root water uptake was uniform along the transect and uncorrelated with canopy structure. The final period from September 26 to October 24 at the end of the growing season, which was characterized by high rainfall amounts (Figure 3.4), coincided with leaf fall-off. Higher throughfall quantities along the transect resulted in disappearance of the correlation between soil moisture and canopy indicators (Figure 5.18), as would be expected. The lower depth intervals showed comparable behavior, although the effect of canopy became less significant with depth. Analysis of the data shows no strong correlation between DBH and the number of trees with soil moisture distribution; this is no surprise as these vegetation variables do not significantly impact interception and throughfall.

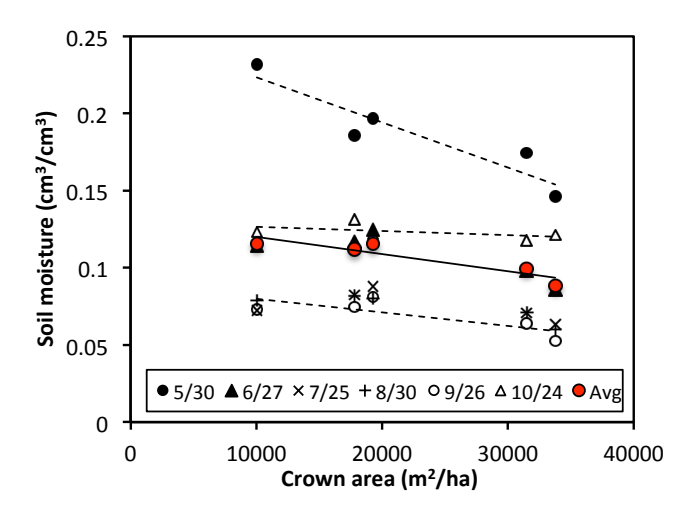


Figure 5.19: Comparison between averaged soil moisture in 5 vegetation quadrats and crown area. Linear regression lines (dashed) are given for datasets on May 30 (first and wettest), September 26 (driest), and October 24 (last), and the average (solid line).

Summary

One of my primary goals of this study was to determine whether the distribution of soil water changes during the growing season. Even though no event-by-event analysis during every big and small rain event was used here, soil moisture data from six tablet periods and monthly water input are analyzed. The results clearly show soil moisture changed with time during growing season and large amount of monthly cumulative precipitaion led to enhanced soil water in October (Figure 5.8). Soil moisture changes at shallow subsurface (0-50 cm) is significant and even in between 100 and 200 cm depth, soil moisutre were still notable. Lowest changes seem to occur in the middle of the five vegetaion quadrats, which had the smallest amount of trees, and thus possibly the least amount of root water uptake are expected. My observation from the six tablet periods suggest that soil moisture distribution changes in a timely manner responding to the changes in throughfall. The behaivor of soil water change is a result of both water input and plant water use. Therefore, soil water does not remain the same during the growing season.

My second goal was to compare soil water with vegetation structure and throughfall and then find out whether they are correlated or not. Figure 5.7 shows that soil wetting areas are related to vegetation parameters such as LAI and number of trees In Figure 5.16, soil moisture change was compared with normalized tablet weight loss. It shows that for most of the months, a correlation between the varibles can be observed unless the changes are too small. The correlation depends on water input and vegetation water use. Figure 5.18 shows a strong correlation between crown area and soil moisture. Crown area is an indicator of canopy structure, similar to LAI. Thus, the spatial variations in soil moisture are related to throughfall

and some vegetation structure in particular crown area and LAI. Number of trees, DBH and basal area had no such impact on soil moisture.

Conclusion

The goal of this research was to improve the understanding of spatial and temporal changes in soil moisture in a deciduous forest. To achieve this goal, a variety of methods were adopted, including Electrical Resistivity Imaging, Throughfall Integrating Funnels, the measurement of soil temperature, leaf-area index measurements, and vegetation surveys.

Electrical resistivity measurements obtained at the study site provide information about the subsurface as reflection of above ground vegetation distribution. Instead of assessing soil moisture distribution solely based on electrical resistivity results, a direct site vegetation survey was conducted. A one-time LAI measurement was collected at the peak of the growing season to provide the information about the canopy structure at the site. Comparing subsurface resistivity outcomes and throughfall results with above surface vegetative cover, strongly suggests that a correlation between soil moisture and vegetation structure exists.

The analysis of using combined methods with both near surface and above ground focus has helped me to find the answers of the two research questions: 1. Soil water changes spatially and temporally during the growing season in a timely manner to water input and vegetative water use and 2. The spatial variations of soil water are correlated to vegetation structure and throughfall. This research has proven the value of ERI for quantifying soil moisture distribution and TIF for capturing throughfall under dense canopy. The results show the significance of the interactions between soil, plant and water.

APPENDICES

APPENDIX A: Inversion Settings

No

Minimum Voltage (mv) 0.02 5.00E-04 Minimum V/I (Ohm) Minimum apparent resistivity (Ohm•m) 1 10000 Maximum apparent resistivity (Ohm•m) Maximum repeat error (%) 3 2 Maximum reciprocal error (%) Remove negative apparent resistivity in ERT data: Yes Remove spikes No

Inversion Method: Smooth model inversion

Vertical axis: Positive Upward

Y Coordinate Depth
Min electrode spacing X (m) 0.03
Min electrode spacing Z (m) 0.03

Keep All Data (no data removal):

Forward Modeling Method: Finite element method Cholesky decomposition

Forward system solver: method Boundary condition type: Dirichlet

Number cells or elements between two electrodes 3 Thickness incremental factor 1 Depth factor 0.5 Max number of iteration of nonlinear inversion 8 Stop RMS error 3% Minimum error reduction between two iterations 2% **Smoothness Factor** 10 **Damping Factor** 10 3 Estimated Noise(%) Minimum resistivity (Ohm•m) 1

Maximum resistivity (Ohm•m) 100000

Horizontal/vertical Roughness ratio 1

APPENDIX B: Tree survey

 Table B.1: Full detail of the tree vegetation survey at sandhill site.

TREE SURVEY FIELD DATA									CALCULATIONS							
Block		Location		Circumference	Crown extent (m)			Ovalitativa Data			t o	STEM		CROWN		
	Tree #	LUCa	tion	Circumerence	Crown extent (III)			Qualitative Data			ld	DBH	Area	Area	apparent	
		Х	У	(m)	S	N	W	Е	tall	dead	wide	deep	(m)	(m^2)	(m^2)	radius (m)
	1	0.7	8.7	0.66	3	1	4.5	0.5	1			1	0.210	0.035	24.0	2.76
	2	1.5	7.3	0.14	1.3	2	1.5	1.5					0.045	0.002	8.0	1.60
1	3	0.8	6.1	0.17	1.9	1.1	1.5	1				1	0.054	0.002	6.3	1.42
1	4	1.15	4.9	0.53	2.5	2	3.5	1.75	1				0.169	0.022	20.1	2.53
	5	3.35	5.35	0.14	1.5	0	1.5	0.9				1	0.045	0.002	4.2	1.15
	6	8.5	2.6	1.9	8	1	4.5	6.5	1		1	1	0.605	0.287	100.1	5.65
	7	11.2	8	2.82	9.5	6.5	9	5.5	1		1	1	0.898	0.633	191.4	7.81
2	8	15.35	3.5	0.1	1.4	0.5	0.6	8.0					0.032	0.001	2.5	0.90
	9	16.3	3.3	1.56	3.8	6	6.5	8	1		1	1	0.497	0.194	123.1	6.26
	10	18.5	0.3	0.22	2.5	1.3	2.8	1.3			1	1	0.070	0.004	13.7	2.09
	11	23.5	1.5	0.1	1.1	0.3	0.8	0.2					0.032	0.001	1.6	0.70
	12	23.2	2	0.18	1.7	1.8	1.8	0.4			1		0.057	0.003	7.5	1.54
3	13	23.65	4.7	1.29	6	4.5	2.5	6.5	1		1	1	0.411	0.132	82.3	5.12
	14	24.3	7	1.68	5.5	4.3	7.5	3.5	1				0.535	0.225	92.1	5.41
	15	24.95	6.8	1.32	0	0	0	0		1			0.420	0.139	0.0	0.00
	16	24.95	8.9	1.27	1.5	4.5	7	1.5	1				0.404	0.128	57.9	4.29
4	17	31.2	6.6	1.15	3.5	5.5	5	6	1	·-	1	1	0.366	0.105	81.3	5.09
	18	43.4	2.3	0.97	5.5	3	3.8	5	1		1		0.309	0.075	61.8	4.44
5	19	44.3	2.1	0.51	0	0	0	0		1			0.162	0.021	0.0	0.00
5	20	44.8	3.1	0.67	2.5	3.5	3	4	1			1	0.213	0.036	34.2	3.30
	21	44.33	6.75	1.29	2.5	5.5	6	2	1				0.411	0.132	60.1	4.37

Table B.1 (Cont'd)

	22	46.7	5.1	1.35	0	0	0	0	1		1		0.430	0.145	0.0	0.00
	23	49.4	0.1	0.77	2.5	5	2	5	1			1	0.245	0.047	47.3	3.88
	24	51.3	1.3	1.08	3.4	4.5	4.2	0.5	1				0.344	0.093	39.0	3.52
6	25	53.9	6.55	0.52	3.8	2.5	1.6	2	1			1	0.166	0.022	21.4	2.61
	26	52.95	8.4	0.74	4	3	2.5	3	1				0.236	0.044	31.6	3.17
	27	52.9	8.5	0.17	1.8	0.7	1.5	0				1	0.054	0.002	4.7	1.22
	28	54.3	6.85	0.18	0.6	0.9	2.5	0.6				1	0.057	0.003	6.1	1.39
	29	55.3	6.5	0.24	0	2	3	0.5			1		0.076	0.005	10.4	1.82
	30	55.4	6.65	0.31	1	1.5	2.5	0.7	1				0.099	0.008	7.8	1.58
	31	55.45	6.9	0.13	0.2	1.2	2.5	0				1	0.041	0.001	6.1	1.39
	32	55	6.7	0.39	0	2.8	2.5	0	1			1	0.124	0.012	11.1	1.88
	33	56.35	5.5	0.32	0	0	0	0		1			0.102	0.008	0.0	0.00
7	34	57.3	4.8	0.89	1.5	3.5	5	2	1		1	1	0.283	0.063	34.2	3.30
	35	57.55	5.3	0.21	0.8	1	3.5	0.3				1	0.067	0.004	11.0	1.87
	36	60.3	6.5	0.98	2	4.5	6	1	1			1	0.312	0.076	48.1	3.91
	37	60.05	5.4	0.43	0	0	5	0			1		0.137	0.015	19.6	2.50
	38	61.7	2.6	0.33	0.3	3.2	4.5	0				1	0.105	0.009	24.0	2.76
	39	62.3	2	0.94	1	5.5	7	1.5	1		1	1	0.299	0.070	64.8	4.54
	40	62	1.35	0.72	2.5	3.5	4	2	1				0.229	0.041	30.2	3.10
8	41	63.5	4	0.67	0	7	0	0		1			0.213	0.036	38.5	3.50
o o	42	64.85	2.45	0.23	0	3	3.3	0		1			0.073	0.004	15.6	2.23

 Table B.2: Summary of vegetation survey in each survey quadrat.

SUMMARY													
Block	# trees	# live trees	stems/ha	DBH (m)	BA	(m²)	CA (m²)						
				average	9x9 m	Hectare	average	9x9 (81m²)	Hectare				
1	6	6	741	0.19	0.35	43.2	27.1	162.7	20084.1				
2	3	3	370	0.48	0.83	102.1	105.7	317.0	39139.0				
3	7	6	864	0.28	0.63	77.9	36.4	255.0	31485.7				
4	1	1	123	0.37	0.11	13.0	81.3	81.3	10035.6				
5	4	3	494	0.27	0.26	32.6	39.0	156.1	19265.5				
6	6	6	741	0.25	0.35	43.5	24.0	144.1	17785.9				
7	13	12	1605	0.15	0.31	38.8	21.0	273.4	33757.6				
8	2	0	247	0.14	0.04	4.9	27.1	54.1	6679.8				

REFERENCES

REFERENCES

- Archie, G. E. (1942), The electrical resistivity log as an aid in determining some reservoir characteristics, Transactions of the American Institute of Mining and Metallurgical Engineers, 146, 54-61.
- Asbjornsen, H., G.R. Goldsmith, M.S. Alvarado-Barrientos, K. Rebel, F.P. Van Osch, M. Rietkerk, J. Chen, S. Gotsch, C. Toboʻn, D.R. Geissert, A. Goʻmez-Tagle, K. Vache, T.E. Dawson, Ecohydrological advances and applications in plant-water relations research: a review (vol 4, pg 3, 2011), Journal of Plant Ecology, 4(3), 192-192.
- Asner, G. P., J. M. O. Scurlock, and J. A. Hicke (2003), Global synthesis of leaf area index observations: implications for ecological and remote sensing studies, Global Ecology and Biogeography, 12(3), 191-205.
- Basso, B., C. Fiorentino, D. Cammarano, G. Cafiero, and J. Dardanelli (2012), Analysis of rainfall distribution on spatial and temporal patterns of wheat yield in Mediterranean environment, European Journal of Agronomy, 41, 52-65.
- Blanco, F. F., and M. V. Folegatti (2003), A new method for estimating the leaf area index of cucumber and tomato plants, Horticultura Brasileira, 21(4), 666-669.
- Borken, W., K. Savage, E. A. Davidson, and S. E. Trumbore (2006), Effects of experimental drought on soil respiration and radiocarbon efflux from a temperate forest soil, Global Change Biology, 12(2), 177-193.
- Bréda, N., A. Granier, F. Barataud, and C. Moyne (1995), Soil water dynamics in an oak stand, Plant and Soil, 172(1), 17-27.
- Breda, N. J. J. (2003), Ground-based measurements of leaf area index: a review of methods, instruments and current controversies, Journal of Experimental Botany, 54(392), 2403-2417.
- Bryant, M. L., S. Bhat, and J. M. Jacobs (2005), Measurements and modeling of throughfall variability for five forest communities in the southeastern US, Journal of Hydrology, 312(1-4), 95-108.
- Carlyle-Moses, D. E., J. S. F. Laureano, and A. G. Price (2004), Throughfall and throughfall spatial variability in Madrean oak forest communities of northeastern Mexico, Journal of Hydrology, 297(1-4), 124-135.

- Crockford, R. H., and D. P. Richardson (2000), Partitioning of rainfall into throughfall, stemflow and interception: effect of forest type, ground cover and climate, Hydrological Processes, 14(16-17), 2903-2920.
- Daily, W., and A. Ramirez (2005), Electrical resistance tomography-theory and practice, Investigation in geophysics, 525.
- Dambrine, E., M. Loubet, J. A. Vega, and A. Lissarague (1997), Localisation of mineral uptake by roots using Sr isotopes, Plant and soil, 192(1), 129-132.
- Dolman, A. J. (1987), Summer and Winter Rainfal Interception in an Oak Forest-Predictions with an Analytical and a Numerical-Simulation Model, Journal of Hydrology, 90(1-2), 1-9.
- Dunkerley, D. (2010), A new method for determining the throughfall fraction and throughfall depth in vegetation canopies, Journal of Hydrology, 385(1-4), 65-75.
- Eustice, B. P. (2011), Exploring the Nature of free Convection in a Sabkha with Electrical Imaging and Hydrological Modeling, Masters' thesis, Michigan State University.
- Fayer, M. J., and D. Hillel (1982), Field Testing of a Two-Dimensional Soil-Moisture Model Simulating Water-Table Fluctions, Soil Science Society of America Journal, 46(2), 396-404.
- Garcia-Montiel, D. C., M. T. Coe, M. P. Cruz, J. N. Ferreira, E. M. da Silva, and E. A. Davidson (2008), Estimating seasonal changes in volumetric soil water content at Landscape scales in a Savanna ecosystem using two-dimensional resistivity profiling, Earth Interactions, 12, 25.
- Gupta, S. C., and R. J. Hanks (1972), Influence of Water-Content on Electrical Conductivity of Soil, Soil Science Society of America Journal, 36(6), 855-857.
- Hadzick, Z. Z., A. K. Guber, Y. A. Pachepsky, and R. L. Hill (2011), Pedotransfer functions in soil electrical resistivity estimation, Geoderma, 164(3-4), 195-202.
- Hansen, M. C., R. S. Defries, J. R. G. Townshend, and R. Sohlberg (2000), Global land cover classification at 1km spatial resolution using a classification tree approach, International Journal of Remote Sensing, 21(6-7), 1331-1364.
- Hayley, K., L. Bentley, M. Gharibi, and M. Nightingale (2007), Low temperature dependence of electrical resistivity: Implications for near surface geophysical monitoring, Geophysical research letters, 34(18), L18402.
- Hayley, K., L. R. Bentley, and M. Gharibi (2009), Time-lapse electrical resistivity monitoring of salt-affected soil and groundwater, Water Resources Research, 45, 14.

- Hayley, K., L. R. Bentley, and A. Pidlisecky (2010), Compensating for temperature variations in time-lapse electrical resistivity difference imaging, Geophysics, 75(4), WA51-WA59.
- Hennig, T., A. Weller, and T. Canh (2005), The effect of dike geometry on different resistivity configurations, Journal of Applied Geophysics, 57(4), 278-292.
- Jayawickreme, D. H. (2008), Exploring the influence of land-use and climate on regional hydrology and groundwater recharge, Ph.D. thesis, 167 pp, Michigan State University, Ann Arbor.
- Jayawickreme, D. H., C. S. Santoni, J. H. Kim, E. G. Jobbagy, and R. B. Jackson (2011), Changes in hydrology and salinity accompanying a century of agricultural conversion in Argentina, Ecological Applications, 21(7), 2367-2379.
- Jayawickreme, D. H., R. L. Van Dam, and D.W. Hyndman (2010), Hydrological consequences of land-cover change: Quantifying the influence of plants on soil moisture with time-lapse electrical resistivity, Geopyhsics, 75(4), WA43-WA50.
- Jayawickreme, D. H., R. L. Van Dam, and D. W. Hyndman (2008), Subsurface imaging of vegetation, climate, and root-zone moisture interactions, Geophysical Research Letters, 35(L18404).
- Keddy, P. A., and C. G. Drummond (1996), Ecological properties for the evaluation, management, and restoration of temperate deciduous forest ecosystems, Ecological Applications, 6(3), 748-762.
- Klaassen, W. (2001), Evaporation from rain-wetted forest in relation to canopy wetness, canopy cover, and net radiation, Water Resources Research, 37(12), 3227-3236.
- LaBrecque, D. J., and X. Yang (2001), Difference inversion of ERT data: A fast inversion method for 3-D in situ monitoring, Journal of Environmental and Engineering Geophysics, 6, 83-89.
- Liu, S. G. (1997), A new model for the prediction of rainfall interception in forest canopies, Ecological Modelling, 99(2-3), 151-159.
- Ma, Y., R. L. Van Dam, and D. H. Jayawickreme (2014), Soil moisture variability in a temperate deciduous forest: insights from electrical resistivity and throughfall data, Environmental Earth Sciences.
- McElrone, A. J., B. Choat, G. A. Gambettam, and C. R. Brodersen (2013), Water uptake and transport in vascular plants, Nature Education Knowledge, 4(5)(6).

- McKenney-Easterling, M., D. R. DeWalle, L. R. Iverson, A. M. Prasad, and A. R. Buda (2000), The potential impacts of climate change and variability on forests and forestry in the Mid-Atlantic Region, Climate Research, 14(3), 195-206.
- Michalzik, B., K. Kalbitz, J. H. Park, S. Solinger, and E. Matzner (2001), Fluxes and concentrations of dissolved organic carbon and nitrogen a synthesis for temperate forests, Biogeochemistry, 52(2), 173-205.
- Michot, D., Y. Benderitter, A. Dorigny, B. Nicoullaud, D. King, and A. Tabbagh (2003), Spatial and temporal monitoring of soil water content with an irrigated corn crop cover using surface electrical resistivity tomography, Water Resources Research, 39(5), 1138.
- Miller, C. R., P. S. Routh, T. R. Brosten, and J. P. McNamara (2008), Application of time-lapse ERT imaging to watershed characterization, Geophysics, 73(3), G7-G17.
- Omonode, R. A., and T. J. Vyn (2006), Spatial dependence and relationships of electrical conductivity to soil organic matter, phosphorus, and potassium, Soil Science, 171(3), 223-238.
- Pepin, S., N. J. Livingston, and W. R. Hook (1995), Temperature-Dependent Measurement errors in Time-Domain Reflectometry Determinations of Soil-Water, Soil Science Society of America Journal, 59(1), 38-43.
- Reed, D., and P. Desanker (1992), Ecological Implications of Projected Climate Change Scenarios in Forest Ecosystems in Northern Michigan, USA, International Journal of Biometeorology, 36(2), 99-107.
- Rein, A., R. Hoffmann, and P. Dietrich (2004), Influence of natural time-dependent variations of electrical conductivity on DC resistivity measurements, Journal of Hydrology, 285(1-4), 215-232.
- Schafer, K. V. R., R. Oren, C. T. Lai, and G. G. Katul (2002), Hydrologic balance in an intact temperate forest ecosystem under ambient and elevated atmospheric CO2 concentration, Global Change Biology, 8(9), 895-911.
- Steelman, C. M., and A. L. Endres (2011), Comparison of Petrophysical Relationships for Soil Moisture Estimation using GPR Ground Waves, Vadose Zone Journal, 10(1), 270-285.
- Topp, G. C., J. L. Davis, and A. P. Annan (1980), Electromagnetic Determination of Soil-water Content Measurements in Coaxial Transmission-lines, Water Resources Research, 16(3), 574-582.
- U.S. Climate (2011), www.weather.com/weather/wxclimatology/monthly/graph/48823.

- Van Dam, R. L. (2012), Landform characterization using geophysics Recent advances, applications, and emerging tools, Geomorphology, 137(1), 57-73.
- Van Dam, R. L. (2013), Calibration functions for estimating soil moisture from GPR dieletric constant measurements, Communications in Soil Science and Plant Analysis. 45(3), 392-413
- Watson, D. J. (1947), Comparative Physiological Studies on the Growth of Field Crops. 1.

 Variations in Net Assimilation Rate and Leaf Area Between Species and Varieties, and Within and Between Years, Annals of Botany, 11(41), 41-76.
- Wen, J. (1999), Evolution of eastern Asian and eastern North American disjunct distributions in flowering plants, Annual Review of Ecology and Systematics, 30, 421-455.
- Western, A. W., G. Bloschl, and R. B. Grayson (1998), Geostatistical characterisation of soil moisture patterns in the Tarrawarra a catchment, Journal of Hydrology, 205(1-2), 20-37.
- Wilhelm, W. W., K. Ruwe, and M. R. Schlemmer (2000), Comparison of three leaf area index meters in a corn canopy, Crop Science, 40(4), 1179-1183.
- Wullschleger, S. D., F. C. Meinzer, and R. A. Vertessy (1998), A review of whole-plant water use studies in trees, Tree Physiology, 18(8-9), 499-512.
- Yamakawa, Y., K. Kosugi, S. Katsura, N. Masaoka, and T. Mizuyama (2012), Spatial and Temporal Monitoring of Water Content in Weathered Granitic Bedrock Using Electrical Resistivity Imaging, Vadose Zone Journal, 11(1), 13.
- Zhou, Q. Y., J. Shimada, and A. Sato (2001), Three dimensional spatial and temporal monitoring of soil water content using electrical resistivity tomography, Water Resources Research, 37(2), 273-285.